Cancer Cell

Article

Immune heterogeneity in small-cell lung cancer and vulnerability to immune checkpoint blockade

Graphical abstract

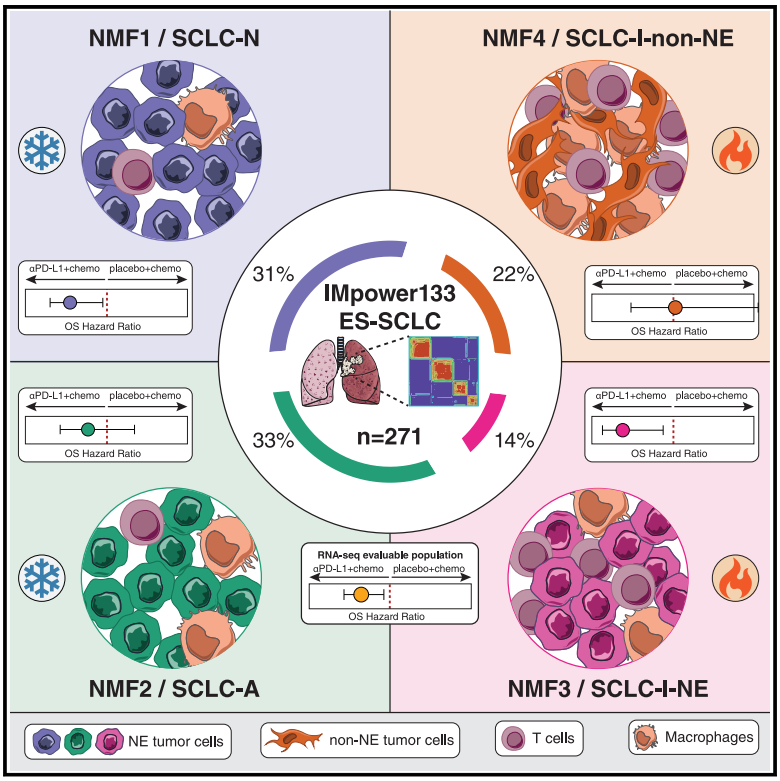

Authors

Barzin Y. Nabet, Habib Hamidi, Myung Chang Lee, ..., Stephen V. Liu, Martin Reck, David S. Shames

Correspondence

nabet.barzin@gene.com (B.Y.N.), shames.david@gene.com (D.S.S.)

In brief

Nabet et al. utilize RNA-seq from a large randomized SCLC clinical trial to identify four patient subsets with distinct neuroendocrine (NE) phenotypes, immune composition, and benefit from immunotherapy. In the two T cell-inflamed subsets, NE tumors with low macrophages benefit from immunotherapy compared to non-NE tumors with high macrophages.

Highlights

- Four subsets of SCLC identified via transcriptomics of clinical trial samples
- Immune-inflamed subsets show both neuroendocrine (NE) and non-NE phenotypes
- Immune-inflamed subsets have heterogeneous immune composition and outcomes
- NE tumors with high T cells and low macrophages benefit from anti-PD-L1 plus chemo

Nabet et al., 2024, Cancer Cell *42*, 1–15
March 11, 2024
https://doi.org/10.1016/j.ccell.2024.01.010

CellPress

Cancer Cell

CellPress

Article

Immune heterogeneity in small-cell lung cancer and vulnerability to immune checkpoint blockade

Barzin Y. Nabet,[1,13,14,*] Habib Hamidi,[1,13] Myung Chang Lee,[1] Romain Banchereau,[1] Stefanie Morris,[2] Leah Adler,[2] Velimir Gayevskiy,[1,3] Ahmed M. Elhossiny,[1] Minu K. Srivastava,[1] Namrata S. Patil,[1] Kiandra A. Smith,[1] Rajiv Jesudason,[1] Caleb Chan,[1] Patrick S. Chang,[1] Matthew Fernandez,[1] Sandra Rost,[1] Lisa M. McGinnis,[1] Hartmut Koeppen,[1] Carl M. Gay,[4] John D. Minna,[5,6,7] John V. Heymach,[4] Joseph M. Chan,[8,9] Charles M. Rudin,[8,9,10] Lauren A. Byers,[4] Stephen V. Liu,[11] Martin Reck,[12] and David S. Shames[1,*]

[1]Genentech Inc., South San Francisco CA, USA
[2]F. Hoffmann-La Roche Ltd, Basel, Switzerland
[3]Rancho Biosciences, San Diego, CA, US
[4]Department of Thoracic/Head & Neck Medical Oncology, The University of Texas MD Anderson Cancer Center, Houston, TX, USA
[5]Hamon Center for Therapeutic Oncology Research, UT Southwestern Medical Center, 6000 Harry Hines Blvd., Dallas, TX 75390-8593, USA
[6]Simmons Comprehensive Cancer Center, UT Southwestern Medical Center, Dallas, TX 75390, USA
[7]Departments of Internal Medicine and Pharmacology, UT Southwestern Medical Center, Dallas, TX 75390, USA
[8]Department of Medicine, Thoracic Oncology Service, Memorial Sloan Kettering Cancer Center, New York, NY 10065, USA
[9]Program for Computational and Systems Biology, Sloan Kettering Institute, Memorial Sloan Kettering Cancer Center, New York, NY 10016, USA
[10]Weill Cornell Medical College, New York, NY 10065, USA
[11]Lombardi Comprehensive Cancer Center, Georgetown University, Washington, DC, USA
[12]Lung Clinic Grosshansdorf, Airway Research Center North, German Center of Lung Research, Grosshansdorf, Germany
[13]These authors contributed equally
[14]Lead contact
*Correspondence: nabet.barzin@gene.com (B.Y.N.), shames.david@gene.com (D.S.S.)
https://doi.org/10.1016/j.ccell.2024.01.010

SUMMARY

Atezolizumab (anti-PD-L1), combined with carboplatin and etoposide (CE), is now a standard of care for extensive-stage small-cell lung cancer (ES-SCLC). A clearer understanding of therapeutically relevant SCLC subsets could identify rational combination strategies and improve outcomes. We conduct transcriptomic analyses and non-negative matrix factorization on 271 pre-treatment patient tumor samples from IMpower133 and identify four subsets with general concordance to previously reported SCLC subtypes (SCLC-A, -N, -P, and -I). Deeper investigation into the immune heterogeneity uncovers two subsets with differing neuroendocrine (NE) versus non-neuroendocrine (non-NE) phenotypes, demonstrating immune cell infiltration hallmarks. The NE tumors with low tumor-associated macrophage (TAM) but high T-effector signals demonstrate longer overall survival with PD-L1 blockade and CE versus CE alone than non-NE tumors with high TAM and high T-effector signal. Our study offers a clinically relevant approach to discriminate SCLC patients likely benefitting most from immunotherapies and highlights the complex mechanisms underlying immunotherapy responses.

INTRODUCTION

Small-cell lung cancer (SCLC) is an aggressive neuroendocrine malignancy that accounts for approximately 15% of all lung cancers.[1–3] SCLC is usually classified into two stages: limited-stage (LS)-SCLC and extensive-stage (ES)-SCLC,[4] and it is estimated that approximately 70% of patients have ES-SCLC at the time of diagnosis.[5] The long-term prognosis of patients with ES-SCLC is poor. While the disease is responsive to chemotherapy, the relapse rate is high, with over 90% of patients with metastatic disease progressing within two years of treatment.

Until recently, the standard first-line treatment for patients with ES-SCLC was carboplatin or cisplatin and etoposide chemotherapy.[6] With the addition of PD-L1/PD-1 (PD-(L)1) blockade to traditional chemotherapy, improvements in overall survival (OS) and progression-free survival (PFS) have been observed in ES-SCLC, as demonstrated by results from global, randomized, phase 3 clinical trials in all-comer populations, such as IMpower133[7,8] and CASPIAN.[9,10] Based on results from IMpower133, atezolizumab in combination with carboplatin and etoposide (CE) was the first immune checkpoint inhibitor approved for first-line treatment of ES-SCLC,[7,8] shifting the treatment paradigm in this disease area. Moreover, the atezolizumab arm of SKYSCRAPER-02 demonstrated similar results to IMpower133, affirming its continued use as a standard of care.[11]

Please cite this article in press as: Nabet et al., Immune heterogeneity in small-cell lung cancer and vulnerability to immune checkpoint blockade, Cancer Cell (2024), https://doi.org/10.1016/j.ccell.2024.01.010

In general, SCLC tumors are considered immunological deserts with low major histocompatibility complex expression, and the tumor cells have low PD-L1 expression, potentially contributing to the relatively modest improvement observed with immunotherapy plus platinum chemotherapy.[8,12] Therefore, a better understanding of the molecular features of SCLC that are associated with response to therapy is necessary to personalize therapeutic strategies.

Based on multiple lines of evidence, including primary human cancers, xenografts, cancer cell lines, and genetically engineered mouse models, the expression of three key transcription factors appears to be associated with specific molecular subtypes of SCLC: achaete-scute homolog 1 (*ASCL1*), neurogenic differentiation factor 1 (*NEUROD1*), and POU class 2 homeobox 3 (*POU2F3*).[13–17] Formerly, the consensus within the SCLC research field was that SCLC cellular subtypes were either neuroendocrine (NE, 70%) or non-neuroendocrine (non-NE, 30%).[14,15] Recently, neuroendocrine SCLC tumors were further molecularly characterized and designated as the SCLC-A subtype (*ASCL1* positive) and the SCLC-N subtype (*NEUROD1* positive).[12,16] Two additional subtypes, the inflamed subtype (SCLC-I) and the *POU2F3* subtype (SCLC-P) also have been described.[12,16–18] The SCLC-I subtype displays epithelial-mesenchymal transition (EMT) and an inflamed phenotype, with high expression of genes related to human leukocyte antigens (HLAs), interferon-γ activation, and immune checkpoints, consistent with the association between EMT and immune-related gene expression.[12] The SCLC-P subtype, driven by the transcription factor *POU2F3*, has been described as a major non-neuroendocrine subtype, as well as having some inflammatory features.[12,16]

The limited availability of SCLC patient samples has hampered deep phenotyping of SCLC. For example, SCLC was not a cancer type selected for profiling by The Cancer Genome Atlas.[19] However, the application of non-negative matrix factorization (NMF) to publicly available RNA sequencing (RNA-seq) data[20] has yielded significant insights into the SCLC subtypes.[12] Transferring these specific classifications to IMpower133 demonstrates that the SCLC-I subtype may have the longest OS with atezolizumab in combination with CE, but each subtype (SCLC-A, -N, -P, and -I) benefits from first-line treatment with immunotherapy in combination with CE.[12,21] The data suggest there are subgroups within these SCLC types that need to be identified.

In the current study, we applied NMF to patient tumor samples from the IMpower133 trial, which contains a significantly larger dataset than prior independent analyses of SCLC cohorts, to identify and characterize cellular subsets of SCLC and further refine previously described subtypes.[12,16] Importantly, we define two inflamed subsets with distinct clinical outcomes to atezolizumab plus CE therapy dependent on the balance of T-effector to tumor-associated macrophage (TAM) infiltration.

RESULTS

NMF-defined subsets in IMpower133 have distinct clinical outcomes

To identify SCLC subsets using an unbiased approach, *de novo* NMF was employed[22] using 271 patient samples from the IMpower133 trial.[7,8,23] This is in contrast to Gay et al., where NMF was utilized to identify subtypes using a discovery set of 81 LS-SCLC samples[20] and samples in IMpower133 were subsequently assigned to these specific subtypes using a hierarchical clustering approach of 1,300 variable genes identified in the discovery set. To determine the optimal number of clusters of the *de novo* NMF clustering on IMpower133 samples, we calculated cophenetic correlation scores for an increasing number of clusters for NMF (Figure 1A, top), which determined that k = 4 was optimal based on the drop-off of the cophenetic correlation from k = 4 to k = 5 as well as the presence of well-defined clusters in the consensus matrix (Figures 1A and S1A). Moreover, the cophenetic correlation was similar for k = 5–8 (Figures 1A and S1A). Distributions of the four NMF-identified patient clusters showed that NMF1 and NMF2 had the most patients, with 31.4% (n = 85/271) and 32.5% (n = 88/271), respectively; while NMF3 and NMF4 had smaller percentages of patients, with 14.4% (n = 39/271) and 21.8% (n = 59/271), respectively (Figure 1B and Table S1).

We then characterized whether there was a correlation between different NMF subsets and clinical outcomes. The distribution of responders (complete response/partial response) and non-responders (stable disease/progressive disease) by best overall response in the IMpower133 RNA-seq biomarker evaluable population (BEP) was similar to that of the overall study population[7] (Figure S1B). NMF4 had relatively fewer responders in the atezolizumab arm, while the NMF3 subset had a somewhat increased response rate in the atezolizumab arm compared with a reduced response rate in the placebo arm (Figure S1B). PFS distribution in the BEP and each NMF subset was relatively similar (Figure S1C). Of note, patients in NMF3 treated with atezolizumab had the longest median PFS (mPFS, 5.47 months), while patients in the NMF4 atezolizumab-treated subset demonstrated the shortest (mPFS, 4.22 months) (Figure S1C). Comparing the OS distribution of the different NMF subsets demonstrated that NMF1 (median OS [mOS], atezolizumab arm: 11.14 months, placebo arm: 9.65 months) and NMF2 (mOS, atezolizumab arm: 10.84 months, placebo arm: 10.02 months) exhibited similar results to the BEP (mOS, atezolizumab arm: 11.37 months, placebo arm: 9.85 months) (Figures 1C–1F). In contrast, NMF3 and NMF4 had markedly distinct outcomes from the other groups (Figures 1G and 1H). The NMF3 subset had a near doubling of mOS with atezolizumab plus CE (mOS, 16.37 months) compared with placebo plus CE (mOS, 8.63 months), while the NMF4 demonstrated limited benefit compared with placebo plus CE (mOS, 9.19 vs. 10.11 months, respectively) (Figures 1C and 1H). The Kaplan-Meier curves further demonstrated the longer OS in the atezolizumab arm of the NMF3 patients (HR, 0.45 [95% CI, 0.22–0.89]) compared with the placebo arm (Figure 1G). We previously demonstrated that the SCLC-P subtype had poor prognosis[12,21] and therefore assessed if this subtype was responsible for any poor outcome associations. The removal of SCLC-P tumors from the analyses did not change the outcome associations observed (Figures S1D–S1E). In total, using the largest samples set to date for *de novo* NMF on samples from the IMpower133 trial, we identified patient subgroups with distinct clinical outcomes.

Please cite this article in press as: Nabet et al., Immune heterogeneity in small-cell lung cancer and vulnerability to immune checkpoint blockade, Cancer Cell (2024), https://doi.org/10.1016/j.ccell.2024.01.010

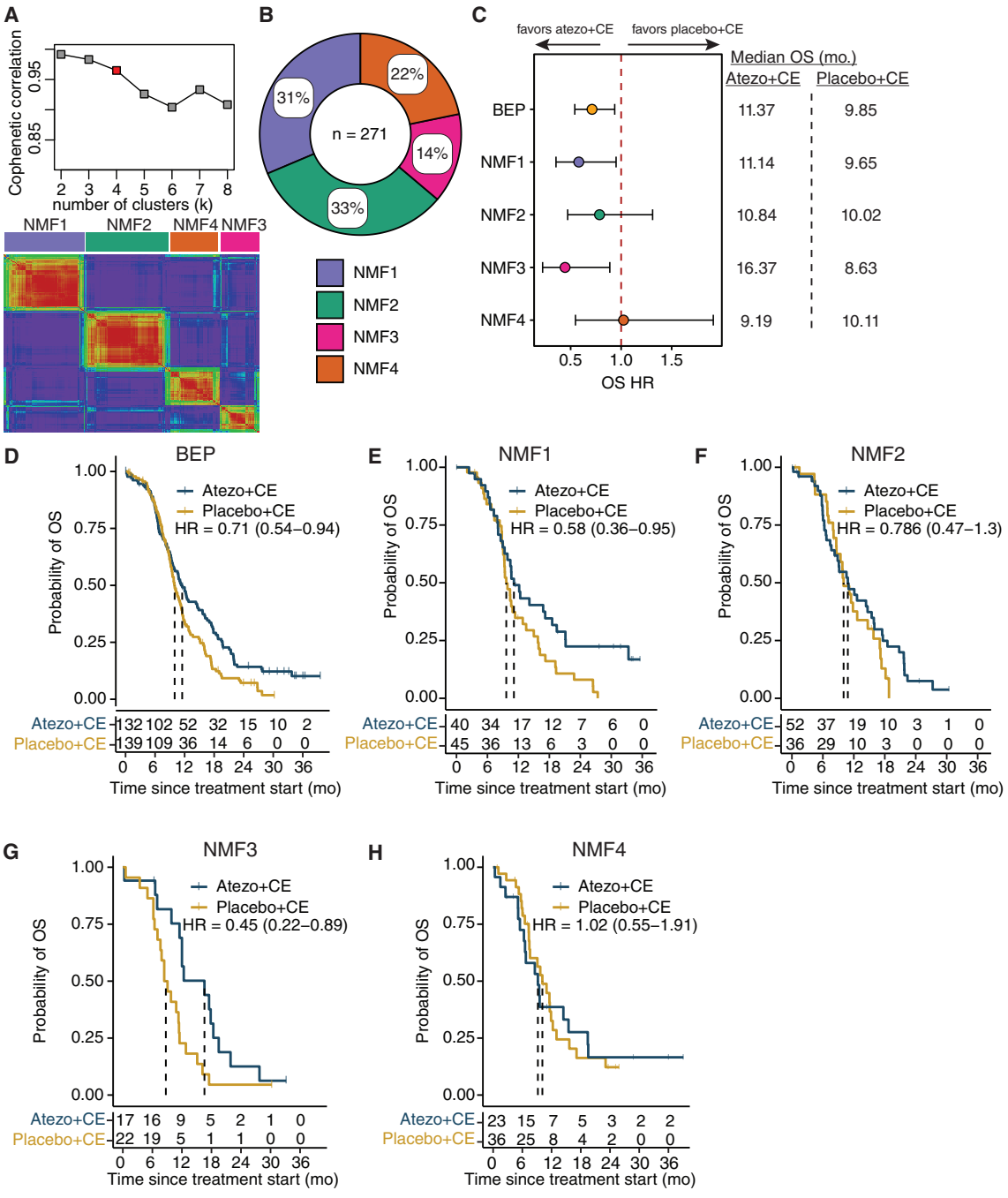

Figure 1. *De novo* NMF of IMpower133 pre-treatment tumor transcriptomes

(A) Cophenetic correlation for increasing number of NMF-defined clusters (top) and consensus matrix for optimal number of clusters (bottom, k = 4).

(B) Relative proportion of each *de novo* NMF-identified subset in IMpower133.

(C) Forest plot depicting the overall survival hazard ratio (OS HR) for atezolizumab+carboplatin/etoposide (Atezo+CE) versus placebo+CE in the biomarker evaluable population (BEP) and each subset. Shown on the right are the median OS for each group, and error bars represent 95% confidence intervals.

(D–H) Kaplan-Meier curves of OS in patients treated with atezolizumab+CE versus placebo+CE in (D) BEP, (E) NMF1, (F) NMF2, (G) NMF3, and (H) NMF4 subsets. OS hazard ratios (HR) and 95% confidence intervals are shown for each subset. Also see Figure S1 and Table S1.

Tumor-intrinsic and microenvironmental determinants of SCLC subsets

To begin identifying molecular distinctions between the four NMF subsets, we performed differential gene expression analyses and gene set analyses comparing each subset to the combination of all other subsets and also to each other (Table S2 and Figure 2A). For gene set analyses, we first considered major components of the tumor microenvironment using curated

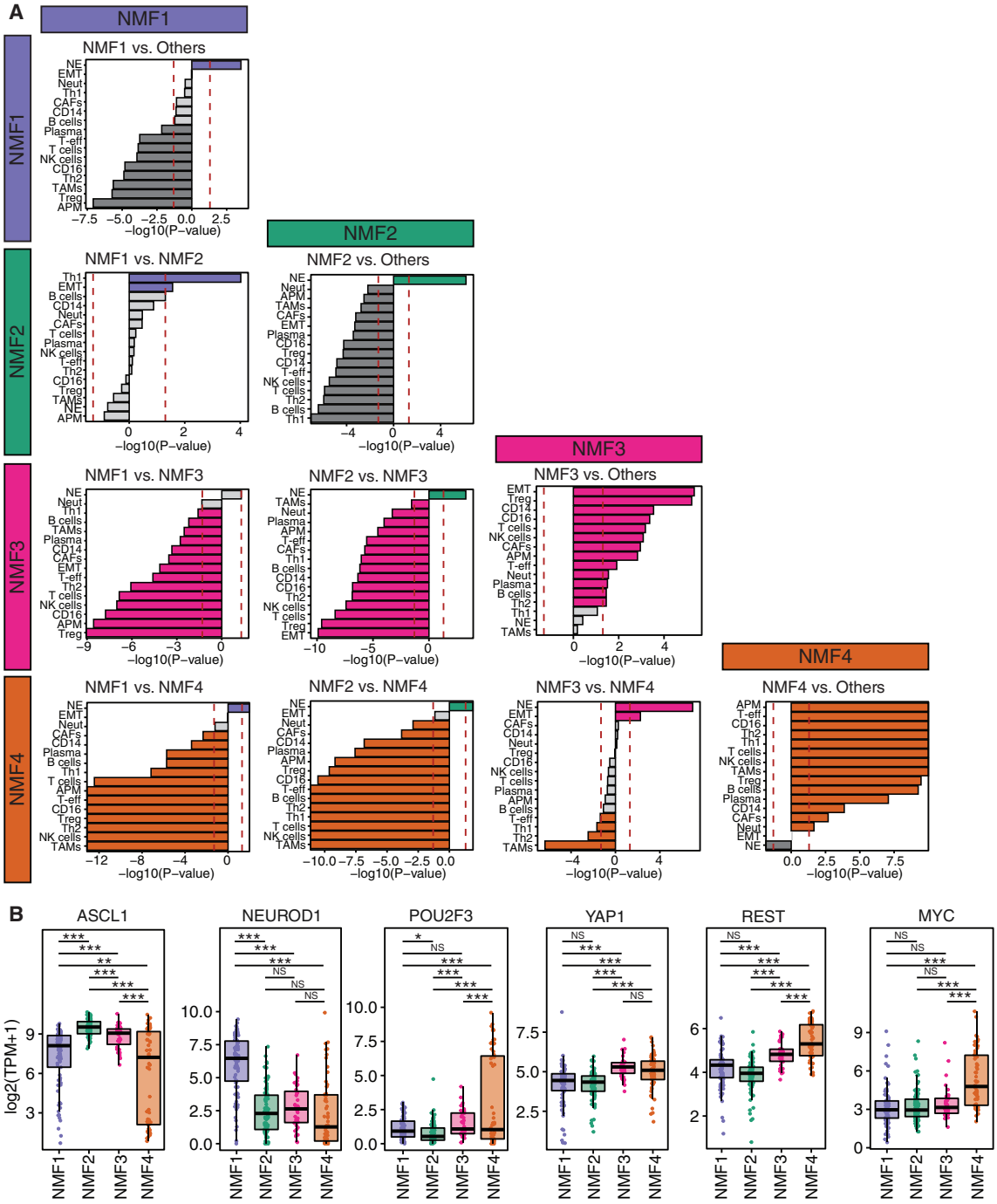

Figure 2. Determinants of *de novo* NMF-defined subsets

(A) One versus all (e.g., NMF1 vs. Others) and pairwise (e.g., NMF1 vs. NMF2) gene set analyses applying gene signatures corresponding to neuroendocrine SCLC (NE), epithelial-to-mesenchymal transition (EMT), cancer-associated fibroblasts (CAFs), tumor-associated macrophages (TAMs), $CD14^+$ monocytes (CD14), $CD16^+$ monocytes (CD16), B cells, plasma cells (Plasma), T cells, T-effector cells (T-eff), NK cells, T regulatory cells (Treg), neutrophils (Neut), Th1 cells (Th1), Th2 cells (Th2), and antigen presentation machinery (APM). Dotted red lines indicate FDR p value = 0.05 while the sign on the x-axis denotes the direction where positive values indicate enrichment in NMF named in column while negative values indicate enrichment in NMF named in the row. For one versus all comparison, negative values indicate enrichment in the other. Bars extending beyond the axis limits indicate p values of 0 (log(P-val) of Infinity). Colors denote FDR p value <0.05 matching the color of the specific subset where the gene signature is enriched, dark gray indicates enrichment in the other in a one versus all comparison, and light gray indicates FDR $p \geq 0.05$.

(B) Boxplots indicating the gene expression of key transcription factors across subsets where each dot represents a unique patient sample. Asterisks denote FDR p values based on differential gene expression analysis of the pairwise comparisons between subsets (Table S2). * FDR $p < 0.05$, ** FDR $p < 0.01$, *** FDR $p < 0.001$, NS FDR $p > 0.05$. Also see Figure S2, Tables S2 and S3.

Please cite this article in press as: Nabet et al., Immune heterogeneity in small-cell lung cancer and vulnerability to immune checkpoint blockade, Cancer Cell (2024), https://doi.org/10.1016/j.ccell.2024.01.010

gene signatures from several sources[24,25] as well as an SCLC neuroendocrine gene signature[17] (Figures 2A and Table S3). Overall, this demonstrated that NMF1, NMF2, and NMF3 had strong NE features, while NMF4 appeared non-NE. NMF3 and NMF4 both have features of enhanced inflammation and antigen presentation machinery when compared to NMF1 and NMF2, suggesting NMF1 and NMF2 are relatively immune desert subsets while NMF3 and NMF4 are relatively immune-inflamed subsets (Figure 2A).

As part of the differential gene expression analysis, we examined each subset's transcription factor expression profiles (Figure 2B and Table S2). NMF2 and NMF3 had the highest *ASCL1* expression, and NMF1 had a uniquely high *NEUROD1* expression (Figure 2B). Prior classification of SCLC-I tumors noted low *ASCL1* expression, suggesting a more neutral subtype. However, our analyses suggest that although NMF3 and NMF4 both show inflamed features, only NMF4 has low *ASCL1* expression, while NMF3 retains high *ASCL1* expression (Figure 2B). *POU2F3* was only expressed in a subset of NMF4, while other drivers of non-NE phenotype, such as RE1-silencing transcription factor (*REST*) and *MYC*, were elevated in more NMF4 tumors compared to other NMF subsets. *YAP1* was similarly elevated in NMF3 and NMF4 and did not uniquely define a subset (Figure 2B). These findings confirm that the previously identified SCLC-P subset may be a portion of a broader non-NE subset, suggesting that non-neuroendocrine SCLC tumors exhibit similar immune landscape and clinical outcomes despite being driven by distinct non-NE drivers.

To uncover potential tumor-intrinsic cell state differences between the *de novo* NMF-defined subsets, we investigated hallmark gene sets.[26] In pairwise comparisons, NMF1 showed evidence of enhanced proliferation and was associated with DNA repair, while NMF3 and NMF4 appeared to be the most mesenchymal (Figure 3A). As expected, based on *MYC* expression, NMF4 had elevated *MYC* target gene expression (Figure 3A). We also investigated previously identified commonly mutated genes in a subset of cases with available whole-exome sequencing[20] and found they were not differentially mutated in each subset (Figure S2A). Copy number analyses of *TP53* and *RB1* showed likely loss in cases where a nonsynonymous mutation did not appear, which suggested inactivation (Figure S2A). Therefore, genotyping did not inform the molecular subset. NOTCH3 mutations were somewhat enriched in NMF3 tumors; however, these mutations did not confer differential hallmark NOTCH signaling (Figures S2B and S2C).

While tumor mutational burden and blood tumor mutational burden (bTMB) have been demonstrated to have potential predictive value for immune checkpoint blockade in several cancer indications, bTMB was not associated with PFS or OS in IMpower133.[7] Here, we also found that the NMF-identified subsets in IMpower133 did not have different bTMB (Figure S2D).

We further compared specific tumor microenvironment (TME) features of the NMF subsets. Individual genes and gene sets corresponding to TME cell types (Figure 3B and Table S2) demonstrated that compared with NMF1 and NMF2, NMF3 and NMF4 showed similarly elevated signature scores for T-effector cells, immune stimulatory molecules, immune inhibitory checkpoints, lymphocytes, total myeloid cells, endothelial cells, and cancer-associated fibroblasts. Although antigen presentation machinery (APM) gene expression was recently identified as a key driver of immune checkpoint blockade therapy benefit,[27,28] stratification of IMpower133 patients using the same APM gene signature from Rudin et al., 2023 did not show significant association with PFS (HR = 1.28 [0.89–1.83]) or OS (HR = 1.2 [0.81–1.77]), likely due to high expression of APM genes in the NMF4 subset which do not benefit from atezolizumab (Figures S3A–S3C). Similarly, immune cell PD-L1 expression, as measured by immunohistochemistry (IHC), was elevated in the two infiltrated subsets (NMF3 and NMF4) compared with the cold subsets (Figure 3C). These data further support that NMF1 and NMF2 can be broadly characterized as immune-cold SCLC and NMF3 and NMF4 as immune-infiltrated SCLC. In total, we identified four subsets with potential therapeutic relevance that are defined by their cell-intrinsic and -extrinsic features. These subsets both recapitulate and suggest heterogeneity within previously reported SCLC features (Figure 3D).

Heterogeneity within established SCLC molecular subtypes

Based on the distribution of known gene expression pathways and prior subtyping classifications, the NMF-identified clusters could be characterized broadly into SCLC-N-enriched, neuroendocrine *NEUROD1*-driven (SCLC-N; NMF1); SCLC-A-enriched, neuroendocrine *ASCL1*-driven (SCLC-A; NMF2); SCLC-I and SCLC-A-enriched, neuroendocrine inflamed (SCLC-I-NE; NMF3); and SCLC-P and SCLC-I-enriched, non-neuroendocrine inflamed (SCLC-I-nonNE; NMF4) (Figure 4A). Prior classification schema identified one inflamed subgroup (SCLC-I), and tentatively identified a second inflamed subgroup SCLC-P (characterized by higher *POU2F3* levels).[12,16,18] Our analysis characterizes two distinct inflamed clusters with the hallmarks of immune cell inflammation and showed that both an NE and a nonNE subgroup were enriched for T cells, B/plasma cells, checkpoint molecules, and APM (Figures 3B–3D and 4A). We compared the distribution of prior subtyping approaches using the single transcription factors (TF subtypes)[16] or the NMF-based subtyping approach (MDACC subtypes)[12] defined for LS-SCLC tumors from a smaller public dataset (George et al., 2015) (Figures S4, 4B, and 4C). Few tumors were classified as a *YAP1* subtype by the TF approach; *YAP1* expression was seen across subsets and was associated with EMT-related gene programs, which confirmed prior studies that suggested it does not exclusively define a subtype.[12,29,30] The SCLC-N subset contained almost all previously identified *NEUROD1* tumors by either approach, the SCLC-A and SCLC-I-NE subsets were both classified as *ASCL1* by the TF approach, and the SCLC-I-nonNE subgroup contained the *POU2F3* tumors using either approach, while the recently identified SCLC-I tumors were split between the SCLC-I-NE and SCLC-I-nonNE subsets. These data suggest that SCLC molecular subsets can be distinguished by both transcription factor drivers and immune infiltration status. Previously reported subtypes can be split into immune-cold and immune-enriched SCLC, where immune-enriched SCLC can be further delineated into SCLC-I-NE and SCLC-I-nonNE based on cell-intrinsic features (Figure 4D). In total, these data recapitulate and extend prior subtyping classifications by uncovering immune heterogeneity within subsets.

Please cite this article in press as: Nabet et al., Immune heterogeneity in small-cell lung cancer and vulnerability to immune checkpoint blockade, Cancer Cell (2024), https://doi.org/10.1016/j.ccell.2024.01.010

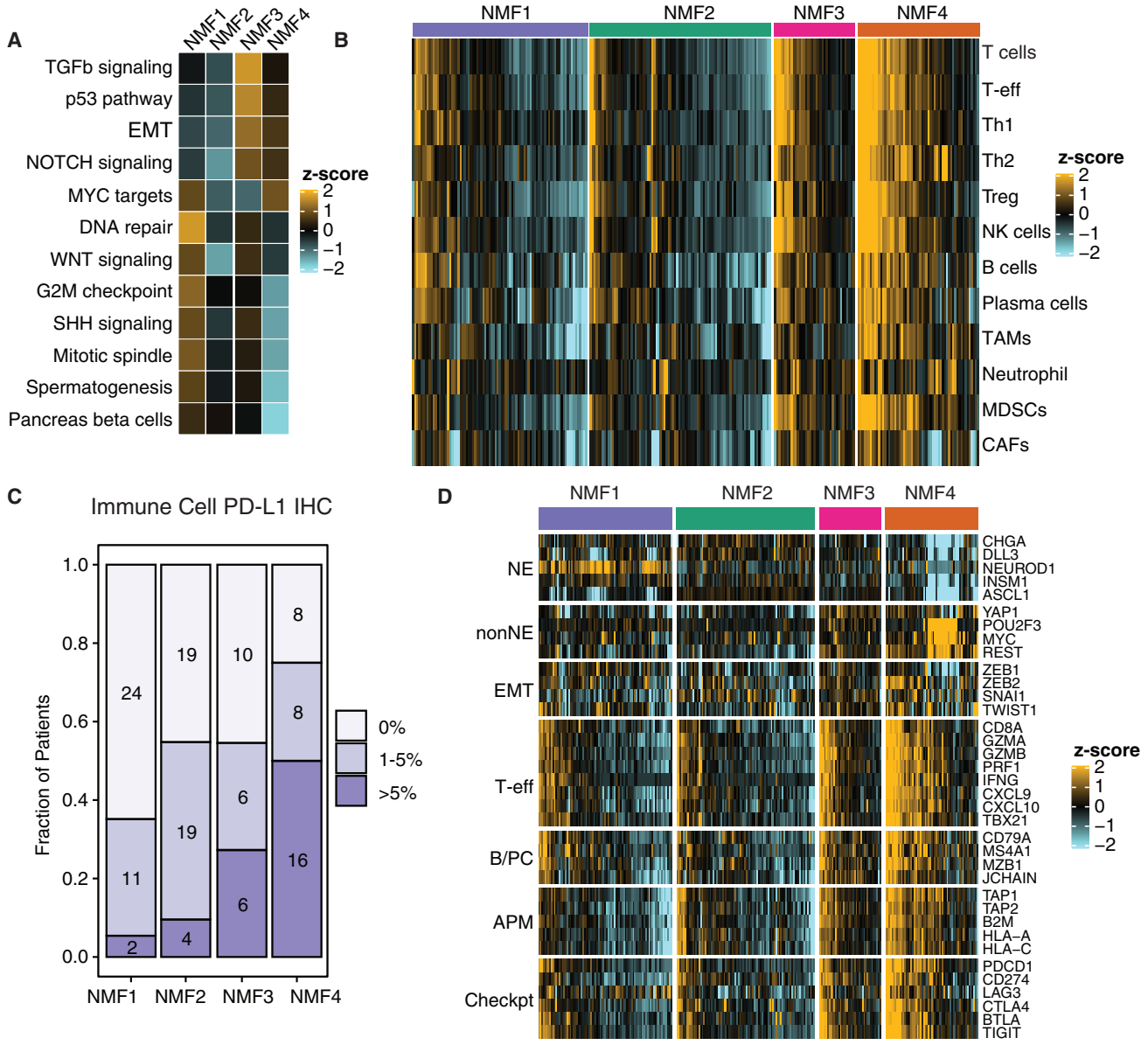

Figure 3. Cell-intrinsic and tumor microenvironmental determinants of *de novo* NMF-defined subsets

(A) Heatmap summarizing Hallmark gene signatures that were significantly enriched in at least one NMF subset by gene set analysis. Shown is the mean gene signature score per NMF subset.

(B) Heatmap of *Z*-scored gene signature scores corresponding to cell types expected to be present in the tumor microenvironment (TME). Each column represents a unique patient sample, and samples are grouped and hierarchically clustered within each subset. MDSCs, myeloid-derived suppressor cells.

(C) Fraction of patients in each NMF subset binned by percentage of pathologist-identified PD-L1-positive immune cells by immunohistochemistry (IHC).

(D) Heatmap of *Z*-scored genes corresponding to cell-intrinsic and TME features. Each column represents a unique patient sample, and samples are grouped and hierarchically clustered within each subset. Also see Figure S3.

Key features of IMpower133 NMF-defined subsets replicate in additional datasets

To examine the generalizability of our NMF-defined subsets, we examined key features in additional datasets and data types. First, we explored the largest available single-cell RNA-seq (scRNA-seq) atlas of human SCLC.[31] Here, we focused on tumor cell gene expression patterns. When examining expression of key transcription factors and APM, we find both NE and non-NE samples with high levels of APM gene expression (Figure 5A). Querying both the key transcription factors and APM, we can classify most samples into the NMF-defined subsets from IMpower133 (Figure 5B), with a minority of samples being unclassified. Hierarchical clustering of single cancer cells using key transcription factors and APM also recovers similar subsets of single cells (Figure S5), where SCLC-A and N-like cells have high expression of *ASCL1* or *NEUROD1* but relatively low APM, SCLC-I-NE cells have high *ASCL1* expression and uniformly high APM expression, and SCLC-I-nonNE-like cells are

Please cite this article in press as: Nabet et al., Immune heterogeneity in small-cell lung cancer and vulnerability to immune checkpoint blockade, Cancer Cell (2024), https://doi.org/10.1016/j.ccell.2024.01.010

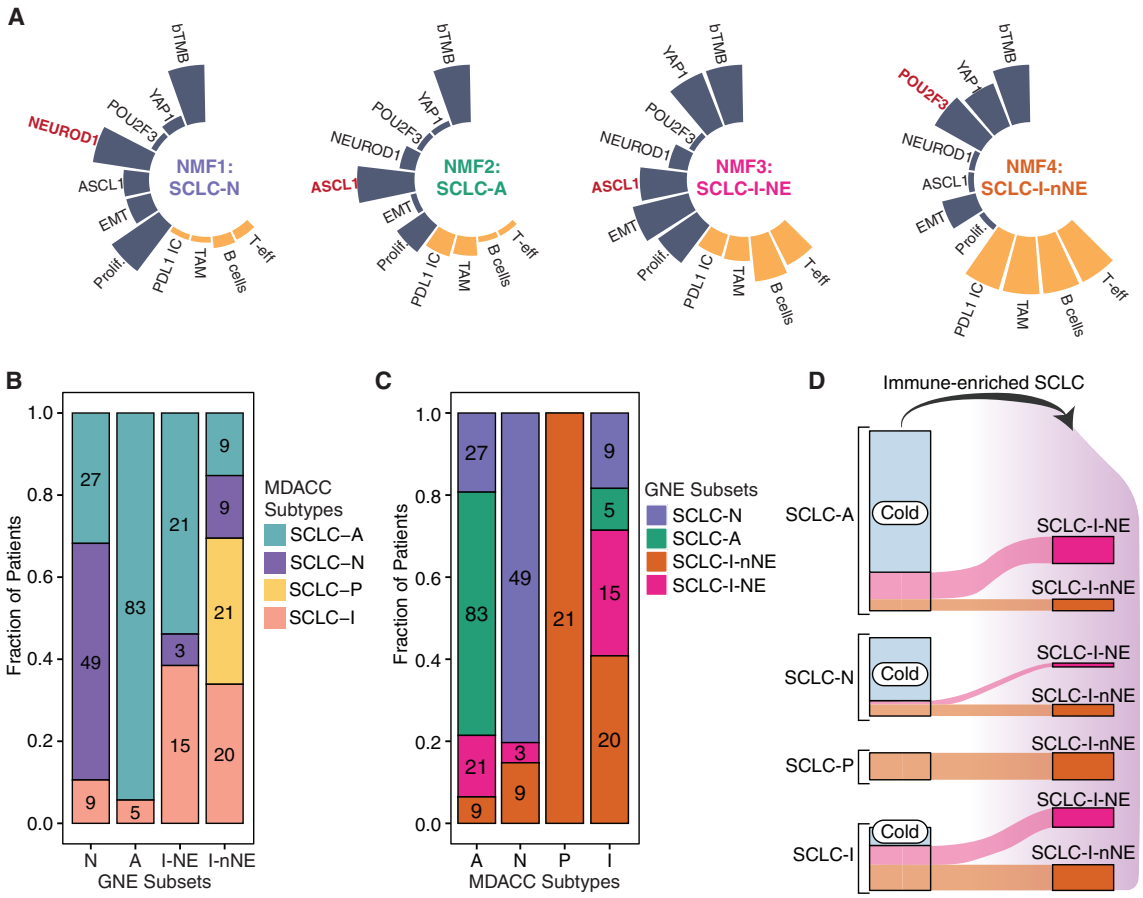

Figure 4. Comparison of IMpower133 NMF-defined subsets to established SCLC subtypes

(A) Radial plot summarizing the defining gene and feature signatures of each *de novo* NMF-defined subset described in the prior figures. The length of each bar corresponds to the relative enrichment (*Z*-score across subsets) of the mean value for each feature. Based on features, NMF1 is *NEUROD1*-driven and immune cold (SCLC-N), NMF2 is *ASCL1*-driven and immune cold (SCLC-A), NMF3 is *ASCL1*-driven and immune hot (SCLC-I-NE), and NMF4 is non-neuroendocrine (including *POU2F3*-driven tumors) and immune hot (SCLC-I-nNE).

(B and C) Representation of the intersection between *de novo* IMpower133 NMF-defined subsets and subsets previously established utilizing unbiased clustering from LS-SCLC RNA-seq (MDACC Subtypes[12]). Shown are the fraction of patients overlapping between each MDACC subtype and the *de novo* IMpower133 NMF-defined subsets.

(D) Heterogeneity of immune-infiltrated SCLC tumors within previously reported (MDACC) subtypes. Immune-infiltrated tumors in each previously reported subtype are classified as SCLC-I-NE or SCLC-I-nonNE. Also see Figure S4.

enriched for *REST* and *POU2F3* expression and have uniformly high APM expression (Figure S5).

We took a similar hierarchical clustering approach to human SCLC cell line bulk RNA-seq available from the Cancer Cell Line Encyclopedia (CCLE) and DepMap.[32,33] Similar to cancer cell scRNA-seq analyses, when setting k = 4, we find subsets that recapitulate the key features of our IMpower133 NMF-defined subgroups. Crucially, there are both NE and non-NE tumors with uniformly high APM gene expression. In total, these data suggest that relevant tumor cell-intrinsic features of the NMF-defined subsets are generalizable beyond IMpower133.

Myeloid infiltration distinguishes inflamed subsets

To distinguish features that may regulate distinct clinical outcomes specifically in the inflamed subsets, we examined the differential gene expression and gene set analysis between SCLC-I-NE and SCLC-I-nonNE tumors (Table S2, Figures 6A and 6B). As previously defined, NE and nonNE genes differentially expressed between these subsets (Figure 6A). We also examined gene sets corresponding to cell types that may make up the SCLC TME and may be differentially associated with each tumor (Figure 6B). Interestingly, we found that while levels of lymphocytes were largely similar, signals of TAMs, which are immunosuppressive macrophages, and the chemokines that may recruit them, were highly enriched in SCLC-I-nonNE tumors compared with SCLC-I-NE tumors (Figure 6B). To further characterize these tumors, we delineated tumors as T-effector (T-eff) cell-high/low and TAM-high/low based on the median cohort-wide expression for these gene signatures. Compared with the non-inflamed subsets (SCLC-N and SCLC-A), the inflamed SCLC-I-NE and SCLC-I-nonNE subsets were both enriched for T-eff-high tumors (≈70%), but the balance of T-eff/TAM signals between the inflamed subsets was markedly different

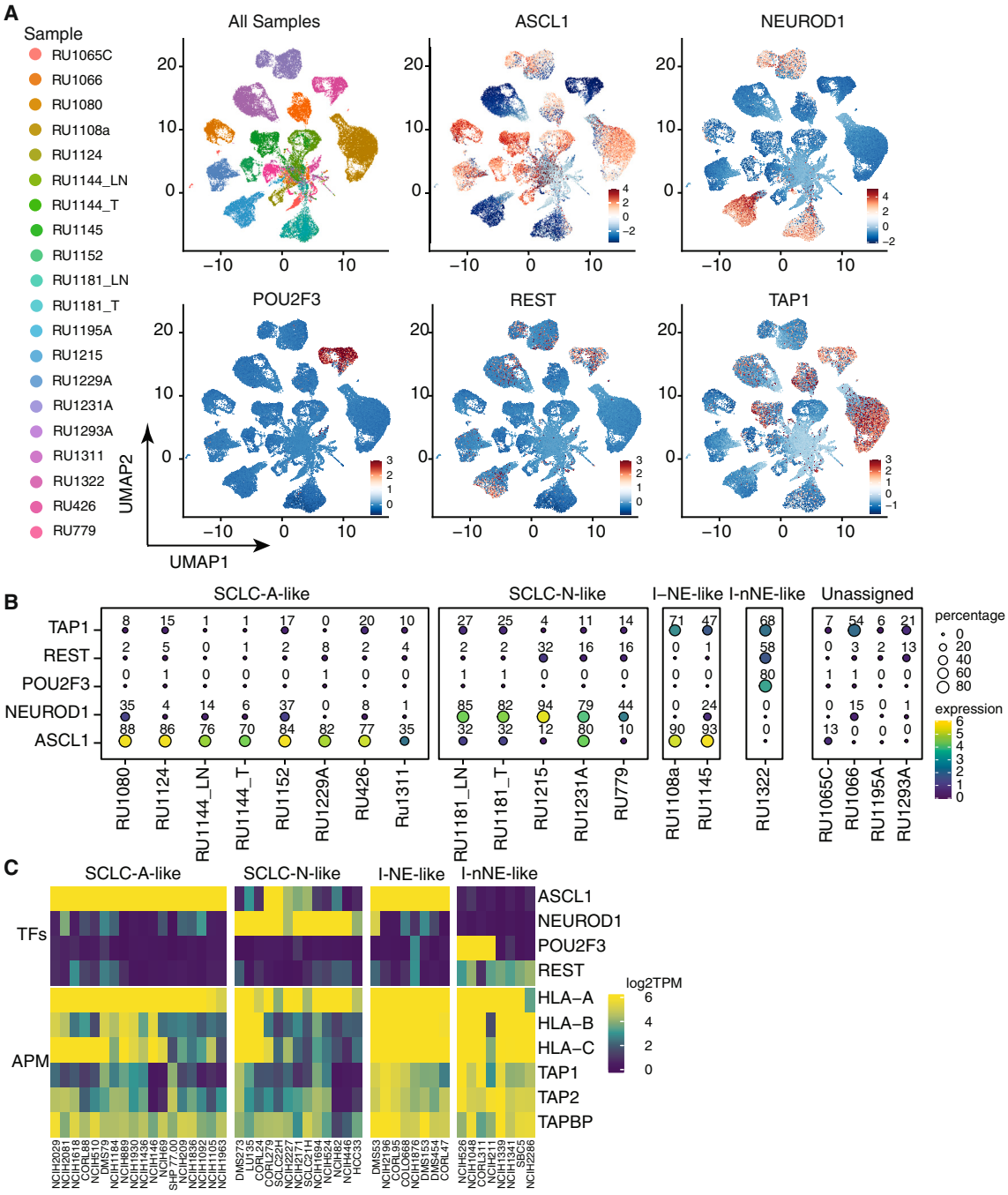

Figure 5. Key features of NMF-defined subsets generalize to other datasets

(A) Non-batch corrected UMAP dimensionality reduction of SCLC cancer cells from previously published human SCLC scRNA-seq atlas.[31] In the top left panel, each cell (dot) is colored by the sample it originated from, while the remaining panels depict normalized expression of key subset-defining transcription factors and TAP1 (representative APM gene).

(B) Bubble plots showing percentage of cells expressing the indicated gene (size) as well as the normalized expression of each indicated gene (color) for cancer cells within each sample from the human SCLC scRNA-seq samples shown in (A). Samples are binned into *de novo* NMF-like subsets based on expression of key NMF subset marker genes highlighted in the earlier figures. Samples without clear enrichment of *de novo* NMF subset-like transcription factor expression were labeled as Unassigned.

(C) Gene expression heatmap of human SCLC cell lines from CCLE/DepMap[32,33] with k = 4 hierarchical clustering for SCLC subset-defining transcription factors and APM genes. Clusters are named based on similarity of key gene expression patterns to IMpower133 NMF-defined subsets. Also see Figure S5.

Please cite this article in press as: Nabet et al., Immune heterogeneity in small-cell lung cancer and vulnerability to immune checkpoint blockade, Cancer Cell (2024), https://doi.org/10.1016/j.ccell.2024.01.010

CellPress

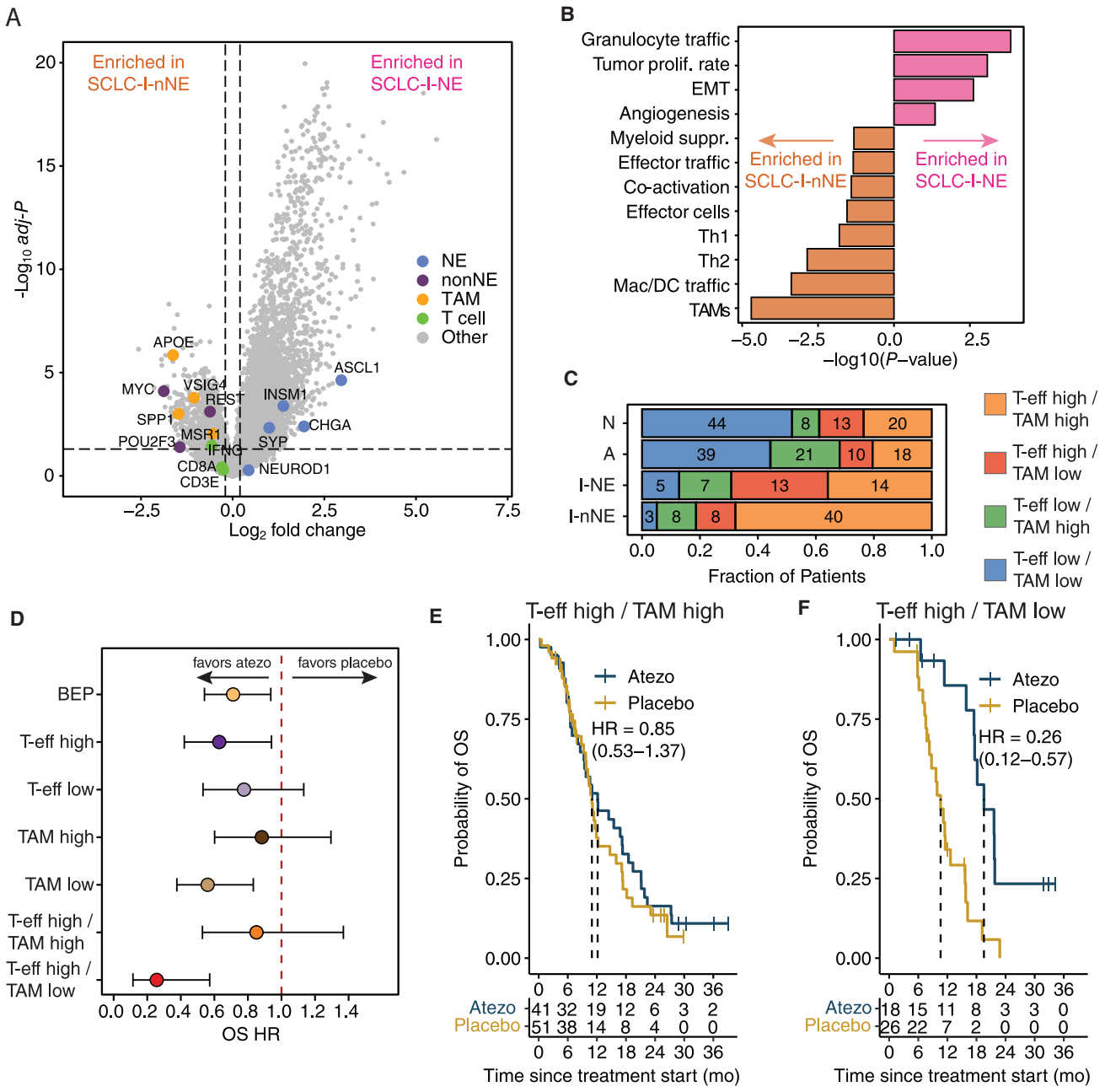

Figure 6. Tumor-associated macrophage signals distinguish inflamed subsets

(A) Volcano plot depicting differentially expressed genes (FDR $p < 0.05$) comparing SCLC-I-nonNE and SCLC-I-NE. Highlighted are genes related to neuroendocrine (NE), non-neuroendocrine (nonNE) phenotype, tumor-associated macrophages (TAM), and T cells.

(B) Gene set analysis of significantly different (FDR $p < 0.05$) tumor and immune-related gene signatures comparing SCLC-I-nonNE and SCLC-I-NE. Sign on the x axis denotes the direction where negative values indicate enrichment in SCLC-I-nonNE and positive values indicate enrichment in SCLC-I-NE.

(C) Overlap of T-effector (T-eff) and TAM-high and -low population (defined by cohort-wide median split for each signature) within each subset.

(D) Forest plot depicting the OS hazard ratio for atezolizumab (atezo)+CE versus placebo+CE in biomarker evaluable population (BEP) and each T-eff/TAM-high and -low subset. Data represent median OS ±95% confidence interval.

(E–F) Kaplan-Meier curves of OS in patients treated with atezolizumab+CE (Atezo) versus placebo+CE (Placebo) in (E) T-eff-high/TAM-high tumors, and (F) T-eff-high/TAM-low tumors. OS hazard ratios (HR) and 95% confidence intervals are shown for each subset. Also see Figure S6.

(Figure 6C). SCLC-I-nonNE tumors that were T-eff-high were almost exclusively also TAM-high, while those that were SCLC-I-NE and T-eff-high were balanced between TAM-high and TAM-low (Figure 6C). To determine whether these signals might correlate with the differential clinical outcomes of atezolizumab plus CE versus placebo plus CE in the inflamed subsets,

Please cite this article in press as: Nabet et al., Immune heterogeneity in small-cell lung cancer and vulnerability to immune checkpoint blockade, Cancer Cell (2024), https://doi.org/10.1016/j.ccell.2024.01.010

we examined the outcomes in the T-eff/TAM subsets. Strikingly, T-eff-high/TAM-low tumors showed additional OS benefit of atezolizumab plus CE compared with all other groups (Figures 6D, S6A, and S6B). Within T-eff-high/TAM-high tumors, which were enriched in SCLC-I-nonNE tumors, atezolizumab plus CE-treated tumors showed similar OS compared to placebo plus CE (HR, 0.85 [95% CI, 0.53–1.37]) (Figure 6E). Within T-eff-high/TAM-low tumors, which were enriched in the SCLC-I-NE subset, atezolizumab plus CE-treated tumors showed markedly longer OS than placebo plus CE-treated tumors (HR, 0.26 [95% CI, 0.12–0.57]) (Figure 6F). In total, these data suggest that differential TAM infiltration may be a clinically relevant determinant of SCLC subsets.

Non-NE signaling is associated with enhanced TAM infiltration

To understand the relative immune cell composition of SCLC tumors beyond bulk transcriptomes, we performed multiplex immunofluorescence on a subset of samples (n = 19) from IMpower133 with available tissue for CD3+/CD8+ T cells, CD3+/CD8- T cells, CD68+/CD163- macrophages, and CD68+/CD163+ macrophages (Figures 7A, 7B, and S7A). Overall, within the pathologist-annotated tumor area, the predominant non-tumor cell type was CD68+/CD163- macrophages (mean = 15.8%, range 6.3%–42.7%) (Figure 7B). As previously demonstrated,[34] T cells were relatively rare within the tumor-annotated regions (mean = 0.6%, range 0.0%–8.0%). Similarly, CD68+/CD163+ macrophages were largely absent from the tumor-annotated regions (Figure 7B). In total, these data suggest that CD68+/CD163- macrophages are a key component of the ES-SCLC microenvironment, but additional deep phenotyping is required to evaluate specific markers/features of these TAMs.

To understand which cell-intrinsic signals may regulate TAM infiltration in inflamed tumors, we assessed which of these features best correlated with TAM signals in T-eff-high tumors in IMpower133. We found that *REST* and *MYC* expression were positively correlated with markers of myeloid infiltration (Figure 7C). To further validate this finding using an independent dataset, additional LS/ES-SCLC samples (n = 58) were procured and analyzed by RNA-seq in order to compare differentially expressed genes between TAM-high and TAM-low tumors within the T-eff-high subset (n = 29) (Figure 7D). We found that relative T cell signals were not distinct in this subgroup (Figure 7D), but *REST* was prominently differentially expressed, while *MYC* was not (Figures 7E and S7B). We further explored whether specific myeloid-related chemokines and cytokines may be upregulated in nonNE tumors by examining differentially expressed genes between NE and nonNE tumors in IMpower133. As expected, due to the high TAM-related signals in IMpower133, we find concomitant elevation of myeloid-related chemokines and cytokines (Figure S7C). To test if this may be related to tumor cell-intrinsic signals, we again examined the bulk RNA-seq dataset of SCLC cell lines available in CCLE/DepMap.[32,33] Here, we find that *REST*, but not *MYC* expression, is highly correlated with several myeloid-related chemokines, such as *CSF1* (Figure S7D). In total, these data suggest a potential role for cell-intrinsic nonNE signaling in recruiting TAMs to the SCLC tumor microenvironment that requires further investigation.

DISCUSSION

Our data show that immune-infiltrated SCLC can be characterized into distinct subsets based on both tumor and immune features and that the balance of these features at baseline is a key determinant of differential outcomes to immune checkpoint blockade. Specifically, tumors with low TAM but high T-eff signals had an NE phenotype and demonstrated longer overall survival with PD-L1 blockade plus CE versus CE alone than did tumors with high TAM and high T-eff signal, which were enriched in the non-NE subset. Until recently, it was thought that all SCLC tumors were neuroendocrine, but the discovery of non-neuroendocrine variants, either lacking *ASCL1/NEUROD1* expression or driven by *POU2F3*, prompted re-evaluation of SCLC classification.[12,16,18,35] Non-neuroendocrine SCLC was initially described as a single subtype.[17,35] However, molecular characterization recently defined two unique non-neuroendocrine SCLC subtypes (SCLC-I and SCLC-P).[12,18] SCLC-P expresses high levels of the transcription factor *POU2F3*, and SCLC-I is characterized by EMT, an inflammatory phenotype, and high expression of genes related to HLAs, interferon-γ activation, and immune checkpoints.[12] More recently, biological subsets of SCLC have been examined through the lens of molecular archetyping, wherein SCLC tumors exist on a continuum across multiple archetype vertices; this approach highlights further the inter- and intra-tumoral heterogeneity observed across SCLC patients.[36] Despite this inter- and intra-tumoral heterogeneity seen in SCLC, however, ES-SCLC patients are treated in an all-comer approach and receive atezolizumab plus CE as a standard of care.

To better understand the SCLC molecular subsets relevant for clinical outcomes to immune checkpoint blockade, we applied *de novo* NMF on IMpower133 RNA-seq data to delineate four subsets (SCLC-N, SCLC-A, SCLC-I-NE, and SCLC-I-nonNE) that demonstrate concordance with prior classification approaches on smaller datasets[12,16,17] but uncover additional heterogeneity in the immune compartment. Similar to previous SCLC classifications, these subsets were categorized into neuroendocrine (SCLC-N, SCLC-A, and SCLC-I-NE) and non-neuroendocrine (SCLC-I-nonNE) phenotypes.[12] In contrast to previous work, we found two inflamed subsets which showed differential neuroendocrine phenotypes: the neuroendocrine SCLC-I-NE subset and the non-neuroendocrine SCLC-I-nonNE subset. The SCLC-I-nonNE subset expressed higher levels of non-neuroendocrine transcription factors, such as *POU2F3*, but did not exclusively contain *POU2F3*-driven tumors, while the SCLC-I-NE subset expressed the transcription factors *ASCL1* and/or *NEUROD1*.

Most significantly, SCLC molecular subsets defined by this work showed differential clinical outcomes to immune checkpoint blockade. Although SCLC-I-NE and SCLC-I-nonNE subsets were both characterized as immune-inflamed subsets and thus would be predicted to show improved response to immunotherapy, only SCLC-I-NE showed significant benefit of atezolizumab compared to placebo while SCLC-I-nonNE patients showed minimal benefit from atezolizumab over placebo treatment. Interestingly, some benefit from atezolizumab plus CE is still observed in the immune cold subsets (SCLC-A and SCLC-N), which could be partially explained by the presence of T-eff high/TAM low samples in these subsets, but the

Please cite this article in press as: Nabet et al., Immune heterogeneity in small-cell lung cancer and vulnerability to immune checkpoint blockade, Cancer Cell (2024), https://doi.org/10.1016/j.ccell.2024.01.010

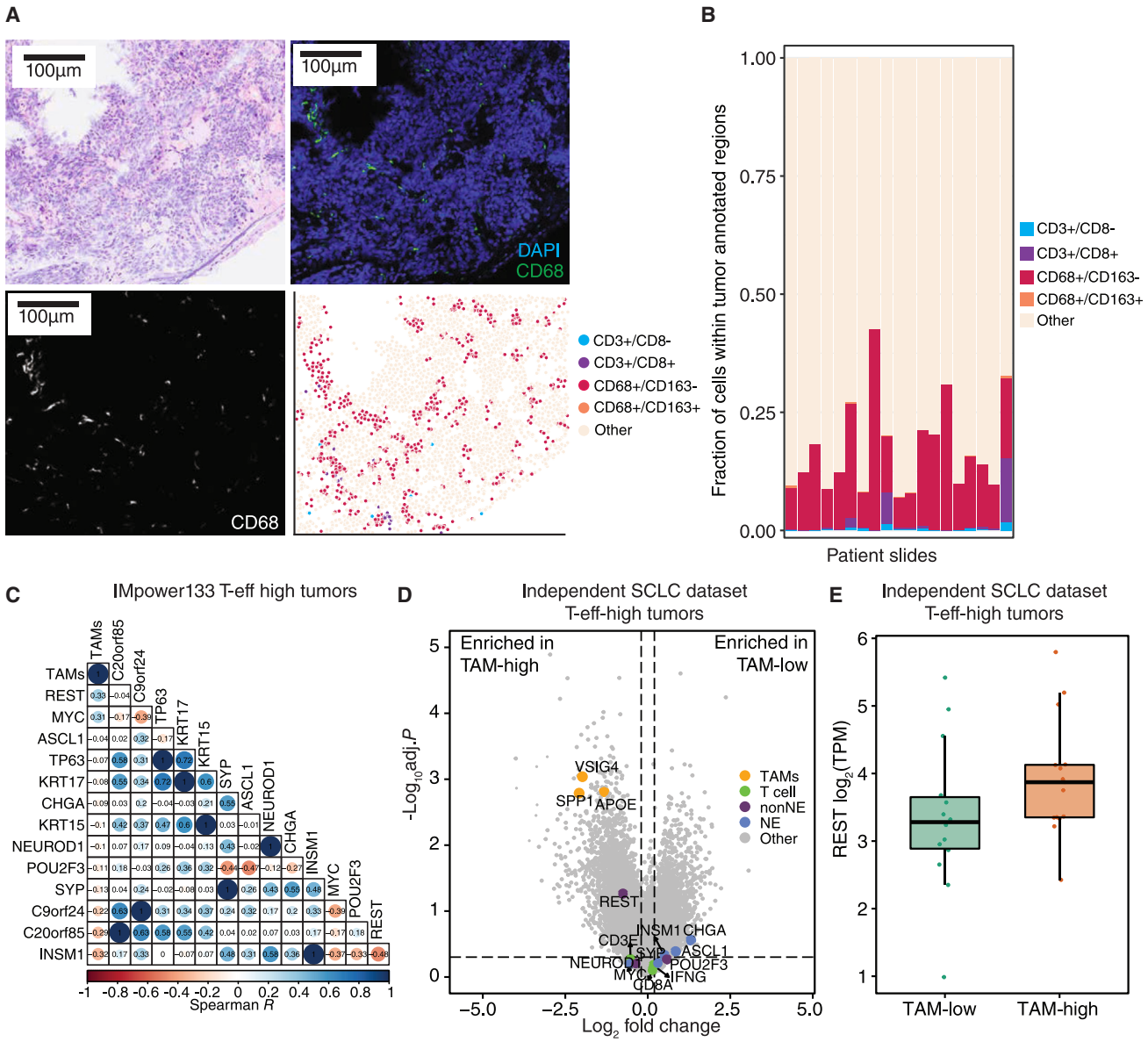

Figure 7. Cell-intrinsic factors may regulate TAM infiltration

(A) H&E (top left), corresponding multiplex immunofluorescence (mIF) for CD68 and DAPI (top right), single channel CD68 (bottom left), and corresponding cell segmentation tissue map incorporating all the phenotypes assayed (bottom right) for a pathologist-annotated tumor region of an average representative SCLC sample from IMpower133. DAPI-segmented cells that were not classified as CD3+/CD8-, CD3+/CD8+, CD68+/CD163+, or CD68+/CD163- were classified as Other. Pathologist review indicated the Other category as predominantly SCLC tumor cells.

(B) Fraction of cells belonging to each mIF-identified phenotype within pathologist-annotated tumor regions from the SCLC sample assayed from IMpower133 (n = 19).

(C) Correlation matrix of SCLC-related genes and TAM signature in the subset of tumors with high T-eff signature score (>median). Rows are ordered based on positive to negative Spearman *R* compared to TAM signature.

(D) Volcano plot depicting differentially expressed genes (FDR p < 0.05) between samples with high TAM-signature scores (n = 14) versus low TAM-signature scores (n = 15) within the T-eff-high tumors in an independently procured SCLC bulk RNA-seq dataset.

(E) *REST* expression in TAM-high versus TAM-low tumors within T-eff-high tumors in the independent SCLC dataset. Also see Figure S7.

mechanisms underlying this response are still unknown and require further investigation. Thus, our approach uncovers subsets that are defined not only by distinct biological pathways driving the tumor phenotype, but also by differential clinical outcomes to immune checkpoint blockade.

Within the immune-enriched subsets, the balance of TAMs and T-eff delineated the response outcome, where patients exhibiting low TAM/T-eff ratios had significantly longer OS with atezolizumab compared to placebo. The four NMF subsets contained patient subgroups with different ratios of TAMs and

Please cite this article in press as: Nabet et al., Immune heterogeneity in small-cell lung cancer and vulnerability to immune checkpoint blockade, Cancer Cell (2024), https://doi.org/10.1016/j.ccell.2024.01.010

T-eff, which may point to a potential tumor-intrinsic control of the immune compartment within SCLC. While we found the expression of nonNE markers to be strongly correlated with TAM signals in T-eff high tumors, validation using an independent dataset implicated that *REST*, more so than *MYC*, is more strongly associated with TAM signals in T-eff-high tumors. To understand which cell-intrinsic programs may be driving high TAM infiltration in T-eff-high tumors, we analyzed publicly available bulk RNA-seq data of SCLC cell lines and demonstrated that *REST* expression is strongly correlated with expression of several key myeloid chemokines and cytokines, such as *CSF1*. While our work suggests a potential link between nonNE phenotype of cancer cells and immunosuppressive TAM phenotype, further investigation is needed to elucidate if and how SCLC cells directly influence the tumor-immune microenvironment.

Recently, it was demonstrated that biomarker-selected studies in ES-SCLC are feasible, establishing the basis for investigating novel treatment strategies in selected ES-SCLC populations.[37] Given that we associate T-eff versus TAM balance and NE versus nonNE tumor pathology as potential predictors of outcomes to immune checkpoint blockade, further investigation and validation are required to evaluate the clinical actionability of these findings. The extent of TAM, T cell, and NE versus nonNE phenotype can be assessed by routine IHC/immunofluorescence, but specific markers, thresholds, and validation of their association with clinical outcomes are required. Using these cell-intrinsic and TME features that we show to be associated with clinical outcomes could form the basis for patient selection or stratification strategies to assess specific combinatorial strategies in the future.

These subsets have significant clinical implications for investigational therapeutics. For example, delta-like ligand 3 (DLL3) expression is highest in the NE subsets (SCLC-A, SCLC-N, and SCLC-I-NE); therefore, use of DLL3 targeting approaches could be tailored to these subsets. For example, non-inflamed neuroendocrine subsets SCLC-A and SCLC-N may be good candidates for DNA damage response-targeting agents, such as DLL3 antibody-drug conjugate therapy.[38] Whereas, T cell engager DLL3 strategies may have the greatest benefit in the SCLC-I-NE subset, while DLL3 targeting approaches should be avoided in the SCLC-I-nonNE subset with minimal DLL3 expression.

When considering therapies for the SCLC-I-nonNE and SCLC-I-NE subsets, the SCLC-I-nonNE subset might benefit from myeloid repolarization agents. In myeloid cell repolarization, TAMs and myeloid-derived suppressor cells are reprogrammed from an immunosuppressive to pro-inflammatory phenotype by stimulation of innate immune pattern recognition receptors, such as TLR7 and TLR8.[39] Since *REST* expression was higher in the SCLC-I-nonNE subset than in the other NMF subsets, another possibility as a potential therapeutic strategy for the SCLC-I-nonNE subset would be to focus a therapy on *REST* target genes. *REST* functions as the transcriptional repressor of neuronal genes in non-neuronal cells to restrict the expression of neuronal genes to the nervous system.[40] Given the associations we observed between nonNE expression and TAM infiltration in two separate SCLC patient cohorts, targeting the nonNE/myeloid axis in SCLC-I-nonNE tumors may be beneficial.

The SCLC-I-NE subset had a larger proportion of patients with high T-eff and low TAM levels compared with other NMF subsets. Therefore, patients in this group may be responsive to blockade of additional immune checkpoints or targeting of T regulatory cells (Tregs). Reducing the activity of immune-inhibiting Tregs could especially benefit the SCLC-I-NE patients who have high levels of immune-activating T-eff and low levels of immune inhibitory TAMs in their tumors.

The results of our study demonstrate the value of deep phenotyping of SCLC to understand response and resistance to current and emerging therapeutic strategies. Although these findings are supported by unbiased profiling of human SCLC in the context of a large phase 3 randomized clinical trial, there are limitations. This study contains the largest collection of SCLC tumor transcriptomes; however, the results presented here require prospective validation in additional randomized clinical trials. Furthermore, while the biological findings are robust across multiple independent datasets, the associations with clinical outcomes are still limited due to small sample size, as 271 patients were divided into 2 treatment arms, each with four molecular subsets. Therefore, as additional SCLC data continue to emerge, we expect the heterogeneous picture of SCLC to continue to evolve and refine.

In conclusion, our study further categorizes the heterogeneity seen in SCLC into four distinct subsets that are defined by both cell-intrinsic and cell-extrinsic factors and clinical response to immune checkpoint blockade. We highlight subsets such as SCLC-I-nonNE, which benefit minimally from immune checkpoint blockade despite showing high immune infiltration, and SCLC-I-NE, which retain NE features and concomitant immune infiltration. The delineation of SCLC heterogeneity offers a clinically relevant approach to distinguish SCLC patients most likely to benefit from current immunotherapeutic approaches, and as new therapeutic strategies emerge, provides a roadmap for personalization of therapy for SCLC.

STAR★METHODS

Detailed methods are provided in the online version of this paper and include the following:

- KEY RESOURCES TABLE
- RESOURCE AVAILABILITY
  - Lead contact
  - Materials availability
  - Data and code availability
- EXPERIMENTAL MODEL AND STUDY PARTICIPANT DETAILS
  - Ethical statement
  - Human tumor specimens
- METHOD DETAILS
  - Study design and participants
  - RNA-seq sample collection and sequencing
  - RNA-seq data generation and processing
  - Bulk RNAseq gene expression analysis and gene set analyses
  - Tumor whole-exome sequencing and variant calling
  - Non-negative matrix factorization (NMF)
  - Multiplex immunofluorescence

- scRNA-seq analysis
- QUANTIFICATION AND STATISTICAL ANALYSIS

SUPPLEMENTAL INFORMATION

Supplemental information can be found online at https://doi.org/10.1016/j.ccell.2024.01.010.

ACKNOWLEDGMENTS

This work was supported by F. Hoffmann-La Roche Ltd /Genentech, Inc, a member of the Roche Group. We thank the patients and their families and the IMpower133 study team and investigators. Medical writing assistance for this manuscript was provided by Michael J. Williams, PhD of Health Interactions and funded by F. Hoffmann-La Roche Ltd. The graphical abstract was partly generated using Servier Medical Art, provided by Servier, licensed under a Creative Commons Attribution 3.0 unported license.

AUTHOR CONTRIBUTIONS

Conceptualization: B.Y.N., H.H., R.B., J.D.M., M.R., S.V.L., and D.S.S.; methodology: H.H. and B.Y.N.; validation: H.H. and B.Y.N.; formal analysis: B.Y.N., H.H., V.G., K.A.S., A.M.E., R.J., C.C., P.S.C., and M.F.; investigation: B.Y.N., H.H., K.A.S., M.R., R.B., S.M., L.A., M.C.L., M.K.S., N.S.P., R.J., C.C., P.S.C., M.F., S.R., L.M.M., H.K., J.M.C., C.M.R., J.V.H., L.A.B., S.V.L., and D.S.S.; resources: M.R., S.V.L., and D.S.S.; data curation: B.Y.N., V.G., K.A.S., and A.M.E.; writing – original draft: B.Y.N., H.H., and D.S.S.; writing – review and editing: all authors; visualization: B.Y.N. and H.H.; supervision: B.Y.N., H.H., and D.S.S.; project administration: B.Y.N. and D.S.S.

DECLARATION OF INTERESTS

B.Y.N., H.H., and D.S.S. are co-inventors on a provisional patent application filed by Genentech/Roche related to this manuscript. B.Y.N. is an employee and stockholder of Roche/Genentech. H.H. is an employee and stockholder of Roche/Genentech. R.B. is an employee and shareholder of Roche/Genentech. S.M. is an employee and shareholder of Roche. L.A. is an employee and shareholder of Roche. V.G. is an employee of Rancho Biosciences and a consultant to Roche/Genentech. M.C.L. is an employee of Roche/Genentech. A.M.E. is an employee of Roche/Genentech. M.K.S. is an employee and shareholder of Roche/Genentech. N.S.P. is an employee and shareholder of Roche/Genentech. K.A.S. is an employee of Roche/Genentech. R.J. is an employee and shareholder of Roche/Genentech. C.C. is an employee and shareholder of Roche/Genentech. P.S.C. is an employee and shareholder of Roche/Genentech. M.F. is an employee of Roche/Genentech. S.R. is an employee and shareholder of Roche/Genentech. L.M.M. is an employee and shareholder of Roche/Genentech. H.K. is an employee and shareholder of Roche/Genentech. J.D.M. receives royalties from the NIH and UTSW for distribution of human tumor cell lines and has the following grants: CA070907, CA213274, and CA213338. C.M.G. reports consulting/advisory fees from AstraZeneca, Bristol Myers Squibb, Catalyst Pharmaceuticals, Daiichi Sankyo, G1 Therapeutics, Insights Driven Research, Jazz Pharmaceuticals, and Monte Rosa Therapeutics, as well as speaking/travel fees from Aptitude Health, BeiGene, DAVA Oncology, MJH, and OncLive, and royalties from UpToDate, Inc. J.M.C. has been paid as a consultant for Sonata Therapeutics and also owns stock in Mirati Therapeutics. J.V.H. has advisory or consulting relationships with Genentech, Mirati Therapeutics, Eli Lilly & Co, Janssen Pharmaceuticals, Boehringer-Ingelheim Pharmaceuticals, Regeneron, Takeda Pharmaceuticals, BerGenBio, Jazz Pharmaceuticals, Curio Science, Novartis, AstraZeneca Pharmaceuticals, BioAtla, Sanofi, Spectrum Pharmaceuticals, GlaxoSmithKline, EMD Serono, Blueprint Medicine, and Chugai Pharmaceuticals. C.M.R. has consulted regarding oncology drug development with AbbVie, Amgen, AstraZeneca, D2G, Daiichi Sankyo, Epizyme, Genentech/Roche, Ipsen, Jazz, Kowa, Lilly, Merck, and Syros. He serves on the scientific advisory boards of Auron, Bridge Medicines, DISCO, Earli, and Harpoon Therapeutics. L.A.B. has consulted regarding oncology drug development Merck Sharp & Dohme Corp., Arrowhead Pharmaceuticals, Chugai Pharmaceutical Co., AstraZeneca Pharmaceuticals, Genetech Inc., BeiGene, AbbVie, Jazz Pharmaceuticals, Puma Biotechnology, Amgen, and Daiichi Sankyo. S.V.L. served as a paid consultant/advisor for oncology drug development with AbbVie, Amgen, AstraZeneca, Bayer, BeiGene, Blueprint, Boehringer-Ingelheim, Bristol-Myers Squibb, Catalyst, AstraZeneca, D2G, Daiichi Sankyo, Eisai, Elevation Oncology Epizyme, Genentech/Roche, Gilead, Guardant Health, Janssen, Ipsen, Jazz Pharmaceuticals, Kowa, Lilly, Merck/MSD, Novartis, Regeneron, Sanofi, Takeda, Turning Point, and Syros. He serves on the scientific advisory boards of Bridge Medicines, Earli, and Harpoon Therapeutics and has received research funding (to institution). M.R. has received honoraria for lectures and consultancy from Amgen, AstraZeneca, BMS, BeiGene, Boehringer-Ingelheim, Daiichi Sankyo, GSK, Mirati, Merck, MSD, Lilly, Novartis, Pfizer, Regeneron, and Sanofi. He has received compensation for membership of DMSB by Daiichi Sankyo and Sanofi. D.S.S. is an employee and stockholder of Roche/Genentech.

Received: July 10, 2023
Revised: December 2, 2023
Accepted: January 23, 2024
Published: February 15, 2024

REFERENCES

1. Früh, M., De Ruysscher, D., Popat, S., Crinò, L., Peters, S., and Felip, E.; ESMO Guidelines Working Group (2013). Small-cell lung cancer (SCLC): ESMO Clinical Practice Guidelines for diagnosis, treatment and follow-up. Ann. Oncol. *24*, vi99–vi105. https://doi.org/10.1093/annonc/mdt178.
2. Gazdar, A.F., Bunn, P.A., and Minna, J.D. (2017). Small-cell lung cancer: what we know, what we need to know and the path forward. Nat. Rev. Cancer *17*, 725–737. https://doi.org/10.1038/nrc.2017.87.
3. van Meerbeeck, J.P., Fennell, D.A., and De Ruysscher, D.K.M. (2011). Small-cell lung cancer. Lancet *378*, 1741–1755. https://doi.org/10.1016/s0140-6736(11)60165-7.
4. Detterbeck, F.C., Nishimura, K.K., Cilento, V.J., Giuliani, M., Marino, M., Osarogiagbon, R.U., Rami-Porta, R., Rusch, V.W., and Asamura, H.; International Association for the Study of Lung Cancer (IASLC) Staging and Prognostic Factors Committee and Advisory Boards (2022). The International Association for the Study of Lung Cancer Staging Project: Methods and Guiding Principles for the Development of the Ninth Edition TNM Classification. J. Thorac. Oncol. *17*, 806–815. https://doi.org/10.1016/j.jtho.2022.02.008.
5. Sabari, J.K., Lok, B.H., Laird, J.H., Poirier, J.T., and Rudin, C.M. (2017). Unravelling the biology of SCLC: implications for therapy. Nat. Rev. Clin. Oncol. *14*, 549–561. https://doi.org/10.1038/nrclinonc.2017.71.
6. Farago, A.F., and Keane, F.K. (2018). Current standards for clinical management of small cell lung cancer. Transl. Lung Cancer Res. *7*, 69–79. https://doi.org/10.21037/tlcr.2018.01.16.
7. Horn, L., Mansfield, A.S., Szczęsna, A., Havel, L., Krzakowski, M., Hochmair, M.J., Huemer, F., Losonczy, G., Johnson, M.L., Nishio, M., et al. (2018). First-Line Atezolizumab plus Chemotherapy in Extensive-Stage Small-Cell Lung Cancer. N. Engl. J. Med. *379*, 2220–2229. https://doi.org/10.1056/nejmoa1809064.
8. Liu, S.V., Reck, M., Mansfield, A.S., Mok, T., Scherpereel, A., Reinmuth, N., Garassino, M.C., De Castro Carpeno, J., Califano, R., Nishio, M., et al. (2021). Updated Overall Survival and PD-L1 Subgroup Analysis of Patients With Extensive-Stage Small-Cell Lung Cancer Treated With Atezolizumab, Carboplatin, and Etoposide (IMpower133). J. Clin. Oncol. *39*, 619–630. https://doi.org/10.1200/jco.20.01055.
9. Paz-Ares, L., Chen, Y., Reinmuth, N., Hotta, K., Trukhin, D., Statsenko, G., Hochmair, M.J., Özgüroğlu, M., Ji, J.H., Garassino, M.C., et al. (2022). Durvalumab, with or without tremelimumab, plus platinum-etoposide in first-line treatment of extensive-stage small-cell lung cancer: 3-year overall survival update from CASPIAN. ESMO Open *7*, 100408. https://doi.org/10.1016/j.esmoop.2022.100408.
10. Paz-Ares, L., Dvorkin, M., Chen, Y., Reinmuth, N., Hotta, K., Trukhin, D., Statsenko, G., Hochmair, M.J., Özgüroğlu, M., Ji, J.H., et al. (2019). Durvalumab plus platinum–etoposide versus platinum–etoposide in

first-line treatment of extensive-stage small-cell lung cancer (CASPIAN): a randomised, controlled, open-label, phase 3 trial. Lancet *394*, 1929–1939. https://doi.org/10.1016/s0140-6736(19)32222-6.

11. Rudin, C.M., Liu, S.V., Soo, R.A., Lu, S., Hong, M.H., Lee, J.-S., Bryl, M., Dumoulin, D.W., Rittmeyer, A., Chiu, C.-H., et al. (2024). SKYSCRAPER-02: Tiragolumab in Combination With Atezolizumab Plus Chemotherapy in Untreated Extensive-Stage Small-Cell Lung Cancer. J. Clin. Oncol. *42*, 324–335. https://doi.org/10.1200/jco.23.01363.
12. Gay, C.M., Stewart, C.A., Park, E.M., Diao, L., Groves, S.M., Heeke, S., Nabet, B.Y., Fujimoto, J., Solis, L.M., Lu, W., et al. (2021). Patterns of transcription factor programs and immune pathway activation define four major subtypes of SCLC with distinct therapeutic vulnerabilities. Cancer Cell *39*, 346–360.e7. https://doi.org/10.1016/j.ccell.2020.12.014.
13. Cardnell, R.J., Li, L., Sen, T., Bara, R., Tong, P., Fujimoto, J., Ireland, A.S., Guthrie, M.R., Bheddah, S., Banerjee, U., et al. (2017). Protein expression of TTF1 and c*MYC* define distinct molecular subgroups of small cell lung cancer with unique vulnerabilities to aurora kinase inhibition, DLL3 targeting, and other targeted therapies. Oncotarget *8*, 73419–73432. https://doi.org/10.18632/oncotarget.20621.
14. Carney, D.N., Gazdar, A.F., Bepler, G., Guccion, J.G., Marangos, P.J., Moody, T.W., Zweig, M.H., and Minna, J.D. (1985). Establishment and identification of small cell lung cancer cell lines having classic and variant features. Cancer Res. *45*, 2913–2923.
15. Gazdar, A.F., Carney, D.N., Nau, M.M., and Minna, J.D. (1985). Characterization of variant subclasses of cell lines derived from small cell lung cancer having distinctive biochemical, morphological, and growth properties. Cancer Res. *45*, 2924–2930.
16. Rudin, C.M., Poirier, J.T., Byers, L.A., Dive, C., Dowlati, A., George, J., Heymach, J.V., Johnson, J.E., Lehman, J.M., MacPherson, D., et al. (2019). Molecular subtypes of small cell lung cancer: a synthesis of human and mouse model data. Nat. Rev. Cancer *19*, 289–297. https://doi.org/10.1038/s41568-019-0133-9.
17. Zhang, W., Girard, L., Zhang, Y.-A., Haruki, T., Papari-Zareei, M., Stastny, V., Ghayee, H.K., Pacak, K., Oliver, T.G., Minna, J.D., and Gazdar, A.F. (2018). Small cell lung cancer tumors and preclinical models display heterogeneity of neuroendocrine phenotypes. Transl. Lung Cancer Res. *7*, 32–49. https://doi.org/10.21037/tlcr.2018.02.02.
18. Huang, Y.-H., Klingbeil, O., He, X.-Y., Wu, X.S., Arun, G., Lu, B., Somerville, T.D.D., Milazzo, J.P., Wilkinson, J.E., Demerdash, O.E., et al. (2018). *POU2F3* is a master regulator of a tuft cell-like variant of small cell lung cancer. Genes Dev. *32*, 915–928. https://doi.org/10.1101/gad.314815.118.
19. Bailey, M.H., Tokheim, C., Porta-Pardo, E., Sengupta, S., Bertrand, D., Weerasinghe, A., Colaprico, A., Wendl, M.C., Kim, J., Reardon, B., et al. (2018). Comprehensive Characterization of Cancer Driver Genes and Mutations. Cell *173*, 371–385.e18. https://doi.org/10.1016/j.cell.2018.02.060.
20. George, J., Lim, J.S., Jang, S.J., Cun, Y., Ozretić, L., Kong, G., Leenders, F., Lu, X., Fernández-Cuesta, L., Bosco, G., et al. (2015). Comprehensive genomic profiles of small cell lung cancer. Nature *524*, 47–53. https://doi.org/10.1038/nature14664.
21. Liu, S.V., Mok, T.S.K., Nabet, B.Y., Mansfield, A.S., De Boer, R., Losonczy, G., Sugawara, S., Dziadziuszko, R., Krzakowski, M., Smolin, A., et al. (2023). Clinical and molecular characterization of long-term survivors with extensive-stage small cell lung cancer treated with first-line atezolizumab plus carboplatin and etoposide. Lung Cancer *186*, 107418. https://doi.org/10.1016/j.lungcan.2023.107418.
22. Skoulidis, F., Byers, L.A., Diao, L., Papadimitrakopoulou, V.A., Tong, P., Izzo, J., Behrens, C., Kadara, H., Parra, E.R., Canales, J.R., et al. (2015). Co-occurring Genomic Alterations Define Major Subsets of KRAS-Mutant Lung Adenocarcinoma with Distinct Biology, Immune Profiles, and Therapeutic Vulnerabilities. Cancer Discov. *5*, 860–877. https://doi.org/10.1158/2159-8290.cd-14-1236.
23. Mansfield, A.S., Każarnowicz, A., Karaseva, N., Sánchez, A., De Boer, R., Andric, Z., Reck, M., Atagi, S., Lee, J.-S., Garassino, M., et al. (2020). Safety and patient-reported outcomes of atezolizumab, carboplatin, and etoposide in extensive-stage small-cell lung cancer (IMpower133): a randomized phase I/III trial. Ann. Oncol. *31*, 310–317. https://doi.org/10.1016/j.annonc.2019.10.021.
24. Bagaev, A., Kotlov, N., Nomie, K., Svekolkin, V., Gafurov, A., Isaeva, O., Osokin, N., Kozlov, I., Frenkel, F., Gancharova, O., et al. (2021). Conserved pan-cancer microenvironment subtypes predict response to immunotherapy. Cancer Cell *39*, 845–865.e7. https://doi.org/10.1016/j.ccell.2021.04.014.
25. Patil, N.S., Nabet, B.Y., Müller, S., Koeppen, H., Zou, W., Giltnane, J., Au-Yeung, A., Srivats, S., Cheng, J.H., Takahashi, C., et al. (2022). Intratumoral plasma cells predict outcomes to PD-L1 blockade in non-small cell lung cancer. Cancer Cell *40*, 289–300.e4. https://doi.org/10.1016/j.ccell.2022.02.002.
26. Liberzon, A., Birger, C., Thorvaldsdóttir, H., Ghandi, M., Mesirov, J.P., and Tamayo, P. (2015). The Molecular Signatures Database Hallmark Gene Set Collection. Cell Syst. *1*, 417–425. https://doi.org/10.1016/j.cels.2015.12.004.
27. Lissa, D., Takahashi, N., Desai, P., Manukyan, I., Schultz, C.W., Rajapakse, V., Velez, M.J., Mulford, D., Roper, N., Nichols, S., et al. (2022). Heterogeneity of neuroendocrine transcriptional states in metastatic small cell lung cancers and patient-derived models. Nat. Commun. *13*, 2023. https://doi.org/10.1038/s41467-022-29517-9.
28. Rudin, C.M., Balli, D., Lai, W.V., Richards, A.L., Nguyen, E., Egger, J.V., Choudhury, N.J., Sen, T., Chow, A., Poirier, J.T., et al. (2023). Clinical Benefit From Immunotherapy in Patients With SCLC Is Associated With Tumor Capacity for Antigen Presentation. J. Thorac. Oncol. *18*, 1222–1232. https://doi.org/10.1016/j.jtho.2023.05.008.
29. Wu, Q., Guo, J., Liu, Y., Zheng, Q., Li, X., Wu, C., Fang, D., Chen, X., Ma, L., Xu, P., et al. (2021). YAP drives fate conversion and chemoresistance of small cell lung cancer. Sci. Adv. *7*, eabg1850. https://doi.org/10.1126/sciadv.abg1850.
30. Shue, Y.T., Drainas, A.P., Li, N.Y., Pearsall, S.M., Morgan, D., Sinnott-Armstrong, N., Hipkins, S.Q., Coles, G.L., Lim, J.S., Oro, A.E., et al. (2022). A conserved YAP/Notch/*REST* network controls the neuroendocrine cell fate in the lungs. Nat. Commun. *13*, 2690. https://doi.org/10.1038/s41467-022-30416-2.
31. Chan, J.M., Quintanal-Villalonga, Á., Gao, V.R., Xie, Y., Allaj, V., Chaudhary, O., Masilionis, I., Egger, J., Chow, A., Walle, T., et al. (2021). Signatures of plasticity, metastasis, and immunosuppression in an atlas of human small cell lung cancer. Cancer Cell *39*, 1479–1496.e18. https://doi.org/10.1016/j.ccell.2021.09.008.
32. Barretina, J., Caponigro, G., Stransky, N., Venkatesan, K., Margolin, A.A., Kim, S., Wilson, C.J., Lehár, J., Kryukov, G.V., Sonkin, D., et al. (2012). The Cancer Cell Line Encyclopedia enables predictive modeling of anticancer drug sensitivity. Nature *483*, 603–607. https://doi.org/10.1038/nature11003.
33. Ghandi, M., Huang, F.W., Jané-Valbuena, J., Kryukov, G.V., Lo, C.C., McDonald, E.R., Barretina, J., Gelfand, E.T., Bielski, C.M., Li, H., et al. (2019). Next-generation characterization of the Cancer Cell Line Encyclopedia. Nature *569*, 503–508. https://doi.org/10.1038/s41586-019-1186-3.
34. Chen, M., Chen, R., Jin, Y., Li, J., Hu, X., Zhang, J., Fujimoto, J., Hubert, S.M., Gay, C.M., Zhu, B., et al. (2021). Cold and heterogeneous T cell repertoire is associated with copy number aberrations and loss of immune genes in small-cell lung cancer. Nat. Commun. *12*, 6655. https://doi.org/10.1038/s41467-021-26821-8.
35. Poirier, J.T., Gardner, E.E., Connis, N., Moreira, A.L., de Stanchina, E., Hann, C.L., and Rudin, C.M. (2015). DNA methylation in small cell lung cancer defines distinct disease subtypes and correlates with high expression of EZH2. Oncogene *34*, 5869–5878. https://doi.org/10.1038/onc.2015.38.
36. Groves, S.M., Ildefonso, G.V., McAtee, C.O., Ozawa, P.M.M., Ireland, A.S., Stauffer, P.E., Wasdin, P.T., Huang, X., Qiao, Y., Lim, J.S., et al. (2022). Archetype tasks link intratumoral heterogeneity to plasticity and

cancer hallmarks in small cell lung cancer. Cell Syst. *13*, 690–710.e17. https://doi.org/10.1016/j.cels.2022.07.006.

37. Abdel Karim, N.F., Miao, J., Reckamp, K.L., Gay, C.M., Byers, L.A., Zhao, Y., Redman, M.W., Carrizosa, D.R., Wang, W.-L., Petty, W.J., et al. (2023). SWOG S1929: Phase II randomized study of maintenance atezolizumab (A) versus atezolizumab + talazoparib (AT) in patients with SLFN11 positive extensive stage small cell lung cancer (ES-SCLC). J. Clin. Oncol. *41*, 8504. https://doi.org/10.1200/jco.2023.41.16_suppl.8504.
38. Owen, D.H., Giffin, M.J., Bailis, J.M., Smit, M.-A.D., Carbone, D.P., and He, K. (2019). DLL3: an emerging target in small cell lung cancer. J. Hematol. Oncol. *12*, 61. https://doi.org/10.1186/s13045-019-0745-2.
39. Pittet, M.J., Michielin, O., and Migliorini, D. (2022). Clinical relevance of tumour-associated macrophages. Nat. Rev. Clin. Oncol. *19*, 402–421. https://doi.org/10.1038/s41571-022-00620-6.
40. Chong, J.A., Tapia-Ramírez, J., Kim, S., Toledo-Aral, J.J., Zheng, Y., Boutros, M.C., Altshuller, Y.M., Frohman, M.A., Kraner, S.D., and Mandel, G. (1995). REST: A mammalian silencer protein that restricts sodium channel gene expression to neurons. Cell *80*, 949–957. https://doi.org/10.1016/0092-8674(95)90298-8.
41. Wu, T.D., Reeder, J., Lawrence, M., Becker, G., and Brauer, M.J. (2016). Statistical Genomics, Methods and Protocols. Methods Mol. Biol. *1418*, 283–334. https://doi.org/10.1007/978-1-4939-3578-9_15.
42. Wu, T.D., and Nacu, S. (2010). Fast and SNP-tolerant detection of complex variants and splicing in short reads. Bioinformatics *26*, 873–881. https://doi.org/10.1093/bioinformatics/btq057.
43. Ritchie, M.E., Phipson, B., Wu, D., Hu, Y., Law, C.W., Shi, W., and Smyth, G.K. (2015). limma powers differential expression analyses for RNA-sequencing and microarray studies. Nucleic Acids Res. *43*, e47. https://doi.org/10.1093/nar/gkv007.
44. Yaari, G., Bolen, C.R., Thakar, J., and Kleinstein, S.H. (2013). Quantitative set analysis for gene expression: a method to quantify gene set differential expression including gene-gene correlations. Nucleic Acids Res. *41*, e170. https://doi.org/10.1093/nar/gkt660.
45. Li, H., and Durbin, R. (2009). Fast and accurate short read alignment with Burrows–Wheeler transform. Bioinformatics *25*, 1754–1760. https://doi.org/10.1093/bioinformatics/btp324.
46. DePristo, M.A., Banks, E., Poplin, R., Garimella, K.V., Maguire, J.R., Hartl, C., Philippakis, A.A., del Angel, G., Hanna, M., Rivas, M.A., et al. (2011). A framework for variation discovery and genotyping using next-generation DNA sequencing data. Nat. Genet. *43*, 491–498. https://doi.org/10.1038/ng.806.
47. Lee, S., Lee, S., Ouellette, S., Park, W.-Y., Lee, E.A., and Park, P.J. (2017). NGSCheckMate: software for validating sample identity in next-generation sequencing studies within and across data types. Nucleic Acids Res. *45*, e103. https://doi.org/10.1093/nar/gkx193.
48. Cibulskis, K., Lawrence, M.S., Carter, S.L., Sivachenko, A., Jaffe, D., Sougnez, C., Gabriel, S., Meyerson, M., Lander, E.S., and Getz, G. (2013). Sensitive detection of somatic point mutations in impure and heterogeneous cancer samples. Nat. Biotechnol. *31*, 213–219. https://doi.org/10.1038/nbt.2514.
49. Wilm, A., Aw, P.P.K., Bertrand, D., Yeo, G.H.T., Ong, S.H., Wong, C.H., Khor, C.C., Petric, R., Hibberd, M.L., and Nagarajan, N. (2012). LoFreq: a sequence-quality aware, ultra-sensitive variant caller for uncovering cell-population heterogeneity from high-throughput sequencing datasets. Nucleic Acids Res. *40*, 11189–11201. https://doi.org/10.1093/nar/gks918.
50. Saunders, C.T., Wong, W.S.W., Swamy, S., Becq, J., Murray, L.J., and Cheetham, R.K. (2012). Strelka: accurate somatic small-variant calling from sequenced tumor–normal sample pairs. Bioinformatics *28*, 1811–1817. https://doi.org/10.1093/bioinformatics/bts271.
51. McLaren, W., Gil, L., Hunt, S.E., Riat, H.S., Ritchie, G.R.S., Thormann, A., Flicek, P., and Cunningham, F. (2016). The Ensembl Variant Effect Predictor. Genome Biol. *17*, 122. https://doi.org/10.1186/s13059-016-0974-4.
52. Brunet, J.-P., Tamayo, P., Golub, T.R., and Mesirov, J.P. (2004). Metagenes and molecular pattern discovery using matrix factorization. Proc. Natl. Acad. Sci. USA *101*, 4164–4169. https://doi.org/10.1073/pnas.0308531101.
53. Li, B., Gould, J., Yang, Y., Sarkizova, S., Tabaka, M., Ashenberg, O., Rosen, Y., Slyper, M., Kowalczyk, M.S., Villani, A.-C., et al. (2020). Cumulus provides cloud-based data analysis for large-scale single-cell and single-nucleus RNA-seq. Nat. Methods *17*, 793–798. https://doi.org/10.1038/s41592-020-0905-x.

Please cite this article in press as: Nabet et al., Immune heterogeneity in small-cell lung cancer and vulnerability to immune checkpoint blockade, Cancer Cell (2024), https://doi.org/10.1016/j.ccell.2024.01.010

STAR★METHODS

KEY RESOURCES TABLE

REAGENT or RESOURCE	SOURCE	IDENTIFIER
Antibodies		
CD68, clone KP-1	Dako	Cat#M0814; RRID: AB_2314148
CD3e, clone SP34-2	BD Pharmingen	Cat#551916; RRID: AB_394293
CD8, clone C8144B	Dako	Cat#M7103; RRID: AB_2075537
CD163, clone EdHu-1	BioRad	Cat#MCA1853; RRID: AB_2074540
Biological samples		
IMpower133 ES-SCLC Samples (n=271)	This study	N/A
Critical commercial assays		
Illumina TruSeq Stranded Total RNA	Illumina	Cat#20020599
SureSelect Human All Exon V6	Agilent	Cat#5190-8872
Deposited data		
Raw and processed RNA-seq data from IMpower133 (n=271).	European Genome-phenome Archive	EGA: EGAS50000000138
Relevant clinical data from IMpower133	European Genome-phenome Archive	EGA: EGAS50000000138
SCLC scRNA-seq	Chan et al.[31]	https://www.synapse.org/#!Synapse:syn23591072
CCLE/DepMap RNA-seq	Barretina et al. and Ghandi et al.[32,33]	https://depmap.org/portal/
Software and algorithms		
R Statistical Software version v4.0.0	The R Foundation	https://www.r-project.org/
survminer package version v0.4.3	CRAN Repository	https://cran.r-project.org/web/packages/survminer/index.html
survival package version v2.42-3	CRAN Repository	https://cran.r-project.org/web/packages/survival/index.html
qusage package v2.18.0	Bioconductor	https://www.bioconductor.org/packages/release/bioc/html/qusage.html
NMF package v0.22.0	CRAN Repository	https://cran.r-project.org/web/packages/NMF/index.html
Pegasus package v1.7.1	Li et al.[53]	https://pegasus.readthedocs.io/en/stable/index.html
Seurat package v.4.4	CRAN Repository	https://cran.r-project.org/web/packages/Seurat/index.html
limma package v3.50.0	Bioconductor	https://bioconductor.org/packages/release/bioc/html/limma.html

RESOURCE AVAILABILITY

Lead contact

Further information and requests should be directed and will be fulfilled by the lead contact, Barzin Nabet (nabet.barzin@gene.com).

Materials availability

This study did not generate new unique reagents.

Data and code availability

For up-to-date details on Roche's Global Policy on the Sharing of Clinical Information and how to request access to related clinical study documents, see here: https://go.roche.com/data_sharing. Anonymized records for individual patients across more than one data source external to Roche cannot, and should not, be linked due to a potential increase in risk of patient re-identification. Raw and processed transcriptomic data and limited clinical data will be made available to qualified researchers at the European Genome-Phenome Archive under accession number EGAS50000000138. To request access to such data, researchers can contact

devsci-dac-d@gene.com. The data will be released to such requesters with necessary agreements to enforce terms such as security, patient privacy and consent of specified data use, consistent with evolving, applicable data protection laws. Additional clinical data is available via request from vivli.org. This paper also analyzes existing, publicly available data, these accession numbers for the datasets are listed in the key resources table.

EXPERIMENTAL MODEL AND STUDY PARTICIPANT DETAILS

Ethical statement

IMpower133 (NCT02763579) is a randomized, Phase I/III, multicenter, double-blinded, placebo-controlled study of atezolizumab (anti–PD-L1) in combination with CE (n=201) compared with treatment with placebo in combination with CE (n=202) in chemotherapy-naive participants with ES-SCLC. The study protocol (Horn et al., 2018) was approved by the institutional review board or independent ethics committee for each study site and was performed in full accordance with the Guideline for Good Clinical Practice and the Declaration of Helsinki.

Human tumor specimens

All biological materials in this study, and subsequent evaluations, were used in accordance with the informed consent agreements obtained from all subjects.

METHOD DETAILS

Study design and participants

The design of the randomized, double-blind IMpower133 trial has been reported previously.[7,8,23] Patients with chemotherapy-naive ES-SCLC were stratified by sex (male versus female), Eastern Cooperative Oncology Group (ECOG) performance status (PS; 0 versus 1), and presence of brain metastases (yes versus no). Patients were randomly assigned 1:1 to receive four 21-day cycles of CE with either intravenous (IV) atezolizumab 1200 mg or IV placebo on day 1 of each cycle (induction phase), followed by IV atezolizumab or placebo (maintenance phase), until unacceptable toxicity or disease progression; patients could continue treatment after progression per Response Evaluation Criteria In Solid Tumors 1.1 (RECIST 1.1) if there was evidence of clinical benefit. Prophylactic cranial irradiation (PCI) was permitted during the maintenance phase. The co-primary endpoints were OS and investigator-assessed PFS in the intention-to-treat population. An independent data and safety monitoring committee reviewed safety data regularly. In this study, tumors from 271/403 (67%) patients were transcriptionally profiled by RNA-seq and tumor mutational burden was profiled by DNA whole exome sequencing (WES).

RNA-seq sample collection and sequencing

Using Hematoxylin and Eosin (H&E) as a guide, formalin-fixed paraffin-embedded tissue (FFPET) was macro-dissected for the tumor area. RNA was extracted using the High Pure FFPET RNA Isolation Kit (Roche) and assessed by Qubit and Agilent Bioanalyzer for quantity and quality. First strand cDNA synthesis was primed from total RNA using random primers, followed by the generation of second strand cDNA with dUTP in place of dTTP in the master mix to facilitate preservation of strand information. Libraries were enriched for the mRNA fraction by depletion of ribsomal RNA. Libraries were sequenced using the Illumina sequencing method.

RNA-seq data generation and processing

TruSeq technology (Illumina) was used to generate whole-transcriptome profiles. To remove ribosomal reads, RNA-seq reads were first aligned to ribosomal RNA sequences. GSNAP version 2013-10-10 was used to align the remaining reads to the human reference genome (NCBI Build 38), allowing a maximum of two mismatches per 75 base sequences (parameters: '-M2-n10-B2-i1-N1-w200000-E1-pairmax-rna = 200000 –clip-overlap).[41,42] To quantify gene expression levels, the number of reads mapped to the exons of each RefSeq gene was calculated using the functionality provided by the R/Bioconductor package GenomicAlignments. Raw counts were adjusted for gene length using transcript-per-million (TPM) normalization, and subsequently log2-transformed. Raw and processed data are available under the data-sharing agreement.

Bulk RNAseq gene expression analysis and gene set analyses

In order to understand the biological pathways underlying NMF-defined subsets, differential gene expression and quantitative set analysis for gene expression (QuSAGE) analysis was performed to compare each cluster to all others and each pairwise comparison. Differentially expressed genes between these two groups were determined using the R package limma, which implements an empirical Bayesian approach to estimate gene expression changes using moderated t-tests.[43] Gene set analyses were performed using the QuSAGE package which quantifies geneset activity with a complete probability density function to then calculate p-values and confidence intervals.[44] Genesets utilized in this study were curated from public repositories and can be found in Table S3. Sample-level gene signature scores for plotting were calculated as the mean z-score for all the genes in the signature across each respective cohort. For Kaplan-Meier analysis of specific gene signatures, samples were dichotomized by the cohort-wide median unless otherwise indicated.

Please cite this article in press as: Nabet et al., Immune heterogeneity in small-cell lung cancer and vulnerability to immune checkpoint blockade, Cancer Cell (2024), https://doi.org/10.1016/j.ccell.2024.01.010

Tumor whole-exome sequencing and variant calling

Whole-exome libraries were prepared from tumor FFPE DNA and matched germline DNA using the Agilent SureSelect v6 and sequenced at 2 x150 bp. Fastq file quality checks were performed with FastQC (v.0.11.9). Fastqs were pre-processed and aligned to hg38 using Picard (v2.18), Burrows-Wheeler Aligner (v0.7.15-r1140),[45] Genome Analysis Toolkit v4.1.4.1.[46] Tumor/normal pair confirmation is provided by NGSCheckmate.[47] Variant calling was done by Mutect2,[48] LoFreq2,[49] and Strelka,[50] and annotated using Ensembl Variant Effect Predictor (VEP).[51] Nonsynonymous variants with a VEP score of moderate or high were only reported if identified by 2 of 3 variant callers.

Non-negative matrix factorization (NMF)

Unsupervised approach based on consensus non-negative matrix factorization (cNMF) was applied to normalized RNAseq data to identify transcriptomic based subsets. This type of clustering is based on the dimensional reduction methodology of NMF which reduces the expression data from thousands of genes to a few metagenes (CRAN. R package version 0.22.0)[52] combined with the consensus clustering to test stability of iterative NMF runs. This method computes multiple k-factor factorization decompositions of the expression matrix and evaluates the stability of the solutions using a cophenetic coefficient. Similar to the approach employed by TCGA in other cancer types, we used a standard non-parametric approach, Median Absolute Deviation (MAD) analysis, to select 5829 genes (top 10%) with the highest variability across 271 tumors.[52] Then, we applied consensus NMF clustering testing k=2 to k=8 and identified k=4 as the most robust subsets using the cophenetic correlation. Earlier work in SCLC[12] determined ~1300 most variable genes using a parametric approach (i.e., standard deviation, in contrast to our non-parametric MAD approach) on 81 LS-SCLC samples from an earlier study[20] to run NMF, while we use our full n=271 ES-SCLC dataset. In the prior work, these ~1300 genes were used to hierarchically cluster IMpower133 samples and assign them to the LS-SCLC-defined subtypes, whereas we *de novo* define subsets in the IMpower133 dataset using NMF.

Multiplex immunofluorescence

5um thick formalin-fixed paraffin-embedded (FFPE) tissue sections were evaluated with multiplex immunofluorescence (mIF) technology for the following markers: CD68 (KP-1; Dako, cat#M0814), CD3e (SP34-2; BD Pharmingen, cat#551916), CD8 (C8144B; Dako, cat#M7103) and CD163 (EdHu-1; BioRad, cat#MCA1853). Panel development and optimization included using 4 micron sections of normal human FFPE tonsil and the results from each experiment were reviewed by the study pathologist. All IF slides were counterstained with DAPI and mounted in Prolong Gold antifade media (Invitrogen, cat# P36930). All scans were performed using the Olympus VS200 at 20X. The chromogenic IHC protocol was adapted for IF on the Ventana Discovery Ultra and checked for signal consistency. The CD68, CD3E, and CD8 antibodies had been previously optimized. An epitope stability assay was performed to determine the best position in a multiplex for the CD163 antibody. During this assay the tissue is subjected to 0-4 elution treatments before the antibody is applied. The fluorescent image signal intensities were quantified via Visiopharm tissue analysis software in order to select the best position for CD163 antibody. An antibody stripping efficiency assay was performed to ensure the antibody was completely eluted after each round of TSA staining. The antibody was titrated and the fluorescence was quantified by Visiopharm software to determine the best concentration, which would provide the brightest signal intensity before diminishing returns. Finally, the entire 4plex including CD163 antibody was tested on the control tonsil tissue along with empty-channel controls (Leave-One-Out) for each antibody.

IMpower133 samples were retrieved from nitrogen storage and stained in two batches due to the capacity limit of the Ventana Discovery Ultra. Both batches included sections of the normal tonsil used in the panel's development for negative and positive controls and to assess inter-batch variation. The stained mIF slides were mounted with Prolong Gold and scanned with the Olympus VS200 at 20X magnification. The slides were then stained for H&E (terminal H&E stain), and the terminal H&E slides were scanned on the Olympus VS200 at 20X.

TSA 4-plex (CD163, CD3e, CD68, and CD8 markers) whole slide images were acquired using immunofluorescence (IF) microscopy on tissue samples that were also H&E-stained and imaged. All images were converted to OME-TIFF format, and image registration between the raw IF and H&E images was performed using the UltiStacker software and uploaded to OMERO for viewing and annotation. Visual inspection of the entire data set was performed by a pathologist, and tumor regions that passed the quality assessment were annotated in OMERO as ROIs for single cell analysis.

The data set was then processed through our Python-based spatial proteomics pipeline for single cell analysis, which includes nucleus segmentation, cell feature extraction, background subtraction, and cell phenotyping. Nucleus segmentation using the DAPI channel of each aligned image was first performed using StarDist's pretrained '2D_versatile_fluo' model, and the mean fluorescent intensity (MFI) of each marker was extracted for each segmented nuclei. Each nuclei was dilated out by a different number of pixels to accommodate for the spatial localization of that specific marker. Each fluorescent marker image was also pre-processed using a median blur filter with a different footprint, depending on the image property of that marker. Background signal reduction for the extracted single-cell MFIs was then independently performed using a Gaussian mixture model (GMM) for each marker, where the MFIs of each cell population within multiple fixed-sized neighborhoods were each fit to a GMM, and a threshold of the background signal was determined between the positive and negative signal clusters. Each single-cell MFI was then corrected for background noise using this threshold. Single-cell phenotyping was then performed by manually determining the global positive signal threshold for each marker, and the phenotype of each cell was then determined based on the marker positivity pattern unique to each cell type. Cells not classified as CD3+/CD8-, CD3+/CD8+, CD68+/CD163+, or CD68+/CD163- were classified as Other. Cells that fall within

the pathologist's annotations were also marked for analysis based on the location of their nucleus centroids. Analyses were restricted to pathologist annotated tumor area.

scRNA-seq analysis

Human SCLC scRNA-seq atlas data[31] were downloaded from Synapse (synapse.org). The Pegasus single cell analysis pipeline (v1.7.1)[53] was used to aggregate samples, then perform quality control to keep high quality samples and cells for further analysis (min_genes = 200, percent_mito = 20, robust genes >= 0.05% of cells), leaving 73,263 cells from 22 samples from 18 patients. Following the standard steps of the Pegasus pipeline built-in marker dictionaries were used to classify inferred clusters into likely cell types, which were manually reviewed for accuracy. Cells were split into tumor and other groups based on cluster membership, and the pipeline was run again for the tumor cells group, followed by a second removal of remaining other cells to leave 57,380 tumor cells. These cells were imported into Seurat v.4.4, where Z scores were calculated for individual genes and plotted on UMAPs with coordinates from Pegasus.

QUANTIFICATION AND STATISTICAL ANALYSIS

R (v4.0.0) was used for all analyses. The two-sided Mann-Whitney test (R function Wilcox.test) for two groups and the Kruskal-Wallis test (R function Kruskal.test) for more than two groups were used for all comparisons for continuous variables, unless otherwise stated. Dunn's post-hoc test was applied with Benjamini-Hochberg multiple testing correction for pairwise comparisons. Pearson's Chi-squared test with continuity correction was used (R function chisq.test) for categorical variables. FDR-adjusted *P*-values are reported. * $P<0.05$; ** $P<0.01$; *** $P<0.001$, unless otherwise stated. Survival analyses were conducted using Cox-proportional hazard models using the R survival package (v3.1.7). Log-rank *P*-values were reported for survival analyses including more than two groups. The horizontal line represents the median in all box plots. The lower and upper hinges in all box blots correspond to the first and third quartiles. The upper whisker extends from the hinge to the largest value no further than 1.5 * IQR from the hinge (where IQR is the interquartile range, or distance between the first and third quartiles). The lower whisker extends from the hinge to the smallest value at most 1.5 * IQR of the hinge.